

Dual-Atom Catalysts for Electrochemical Energy Technologies

Tianchen Cui, Qiming Liu, and Shaowei Chen*

Rational design and engineering of high-performance, low-cost electrocatalysts represents a critical first step in the development of sustainable energy technologies. While single-atom catalysts (SACs) have emerged as viable candidates, recent research has shown that the structure and activity can be further manipulated and enhanced by the incorporation of a second metal center in the close proximity, forming a binuclear configuration. Such dual-atom catalysts (DACs) are recognized as feasible choices to break the limitations of SACs due to the synergetic effects between the bimetallic atoms and their special structures. Herein, the recent advances of DAC electrocatalysis for a range of important reactions, focusing on their synthesis, characterization, and performance, are summarized. The review is concluded with a perspective highlighting the challenges and future research directions.

1. Introduction

Development of renewable and sustainable energy technologies has become an important direction in the field of catalysis and energy research, such as fuel cells, electrolyzers, and metal–air batteries, where electrocatalysts constitute a core component of the electrode structure.^[1–5] Whereas precious metal-based materials have been the catalysts of choice, their high costs and limited natural abundance have significantly limited the widespread applications of these technologies. Thus, development of high-performance, low-cost alternatives has been the focus of research in recent decades. Among these, single-atom catalysts (SACs)^[6–9] have been attracting particular attention, which contain isolated metal atoms embedded within a select functional scaffold. SACs were first demonstrated in 2011 by Zhang et al.^[10] where they synthesized a catalyst consisting of isolated Pt atoms uniformly dispersed on an iron oxide (FeO_x) support of a high surface area, and observed a high activity toward both CO oxidation and preferential oxidation reactions. In numerous subsequent studies, the high activity and selectivity of SACs have been found to arise primarily from the unique electronic structure and 100% atom utilization, in


comparison to the traditional nanoparticle-based counterparts.^[6] This is mainly attributed to the coordination configuration of the metal atoms that dictates the adsorption energetics of key reaction intermediates. However, at least two key challenges remain in the development of SACs. First, because of a surface energy significantly higher than that of the corresponding metal clusters and nanoparticles, aggregation of the single-metal atoms is energetically preferred, leading to reduced electrocatalytic activity and durability.^[11] To mitigate this impact, the metal loading of SACs is typically limited to a low value (≈ 2 wt%)^[12]; yet this compromises the overall performance.

In addition, it is difficult to break the linear scaling relationships between the adsorption energies of reaction intermediates on SACs, such that the catalytic performance of SACs is typically limited in sophisticated reactions with various intermediates. Notably, these issues can be effectively addressed by the incorporation of a second metal center in the close proximity forming dual-atom catalysts (DACs).^[13]

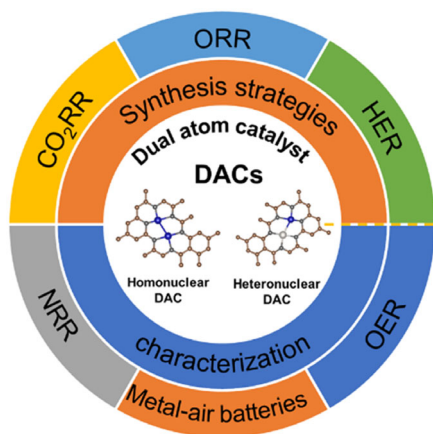
There are two types of DACs. In heteronuclear DACs, two atoms of different metal elements are situated within a functional moiety, whereas in homonuclear DACs, the two metal atoms are of the same element. In these dimeric arrangements, the two atomic centers work cooperatively, optimize the d-band center, and manipulate the spin states of the active sites, leading to an enhanced catalytic activity.^[14,15] Moreover, the multiple-active sites of DACs can support various adsorption configurations which may facilitate the complex reaction pathways of the electrochemical reactions.^[16,17] Recent studies have shown that such a level of structural engineering is uniquely effective in manipulating the electronic properties of the materials and hence the electrocatalytic activity toward a range of reactions that are key to various electrochemical energy technologies, such as hydrogen evolution reaction (HER) and oxygen evolution reaction (OER) in electrochemical water splitting (water electrolyzers), oxygen reduction reaction (ORR) in fuel cells and metal–air batteries, CO₂ reduction reaction (CO₂RR) and nitrogen reduction reaction (NRR) to fuels and other valuable chemicals, among others.

In this review, we will first highlight key procedures for the synthesis of DACs, followed by experimental determination of their atomic configurations and electrochemical performances in various important reactions (**Scheme 1**). We will conclude the review with a perspective highlighting the remaining critical challenges and future research directions.

T. Cui, Q. Liu, S. Chen
Department of Chemistry and Biochemistry
University of California
1156 High Street, Santa Cruz, CA 95064, USA
E-mail: shaowei@ucsc.edu

 The ORCID identification number(s) for the author(s) of this article can be found under <https://doi.org/10.1002/ente.202201456>.

DOI: 10.1002/ente.202201456



Scheme 1. Schematic of DAC preparation, characterization, and applications.

2. Synthesis Strategies and Structural Characterization

2.1. Materials Synthesis

A range of experimental protocols have been developed for the synthesis of DACs, such as atomic layer deposition (ALD),^[18–21] wet chemical adsorption,^[22,23] thermal treatment,^[24–26] among others. In ALD, an ultrathin film of ultrafine particles at the atomic level is deposited onto a select substrate surface, which can be used for the controllable design and synthesis of electrocatalysts.^[27] For example, Zhang et al.^[21] prepared a PtRu DAC supported on nitrogen-doped carbon nanotubes (NCNTs) by using a two-step ALD process. Experimentally, trimethyl(methylcyclopentadienyl)platinum(IV) (MeCpPtMe₃) was used as the precursor and deposited onto NCNTs by chelating to the N dopants during the first ALD process, where the strong metal-support interaction stabilized the formation of Pt single-atom (SA) sites. PtRu DACs were then obtained by a second ALD with bis(ethylcyclopentadienyl) ruthenium(II) as the precursor. Tian et al.^[23] reported a “precursor-preselected” wet-chemistry strategy to prepare Fe₂ DAC supported on mesoporous graphitic carbon nitride (Fe₂/mpg-C₃N₄). While these procedures are rather efficient and facile in sample preparation, ALD generally entails expensive and sophisticated instrumentation, whereas DAC samples prepared by wet chemical adsorption typically suffers from low structural stability.

Within this context, high-temperature heat-treatment methods (HTHM)^[28–30] have emerged as powerful alternatives. Xiao et al.^[31] prepared atomically dispersed FeCu–nitrogen-doped carbon (NC) nanocomposites containing FeN₄ and CuN₄ dual-active sites by HTHM through a classical host–guest strategy, where Fe- and Cu-codoped zeolitic imidazolate frameworks (FeCu–ZIF) were subjected to pyrolysis at 950 °C in a N₂ atmosphere (Figure 1a). The dual-atom structure was confirmed by high-angle annular dark-field scanning transmission electron microscopy (HAADF-STEM) and X-ray absorption spectroscopy (XAS) measurements. Electrochemically, the ORR half-wave potential ($E_{1/2}$) in alkaline media was nearly 40 mV higher than that

of commercial Pt/C and 24 mV higher than that of single-metallic Fe–NC counterparts; and the peak power density of the FeCu–NC-based hydroxide exchange membrane fuel cell (HEMFC) was 0.91 W cm^{−2}, which was 21% higher than that based on Fe–NC (0.76 W cm^{−2}). Density-functional theory (DFT) calculations showed that the introduction of CuN₄ downshifted the d-band center of Fe in FeN₄–CuN₄, weakened the adsorption of OH* on Fe, and therefore improved the catalytic activity. The strain effect caused by the adjacent carbon environment in which the CuN₄ species replaced the FeN₄ species became more significant when the CuN₄ species were situated closer to the FeN₄ moiety, which optimized the electronic structure and improved the catalytic activity. Computation based on the Crystal Orbital Hamilton Population (COHP) theory showed that the d_{xz} , d_{yz} , and d_{z^2} orbitals indeed determined the catalytic activity of the active sites. This work provided a unique insight into the design and synthesis of DACs and the synergistic catalysis of dual-atom sites for ORR.^[31]

Yang et al.^[32] prepared O-coordinated W–Mo heterodimers embedded in N-doped graphene (W₁Mo₁-NG) DACs through a three-step procedure (Figure 2). First, a mixed solution of Na₂WO₄·2H₂O and (NH₄)₆Mo₇O₂₄·4H₂O, and graphene oxide (GO) in water was used as the precursor solution, and hydrothermal treatment at 190 °C for 12 h led to the formation and anchoring of pairs of W–Mo species onto partially reduced GO (p-RGO). The homogeneous mixture was then freeze-dried to minimize restacking of the p-RGO nanosheets. Finally, W₁Mo₁-NG DACs were obtained by chemical vapor deposition treatment in an NH₃/Ar atmosphere at 800 °C, which exhibited a Pt-like activity and ultrahigh stability toward HER in a wide range of electrolyte pH. Mechanistically, the electronic delocalization of the W–O–Mo–O–C configuration was found to offer an optimal adsorption strength of H, boosted the HER kinetics, and promoted the intrinsic activity.

Selection of the supporting substrate materials is also important in the successful preparation of DACs, which dictates the interactions between the metal atoms and the supporting scaffold and hence the structural integrity of DACs.^[33] Nitrogen-doped carbon has been known to help prevent metal atoms from aggregation and corrosion, leading to improvement of the catalyst durability. Yu et al.^[34] reported a strategy that included polydopamine (PDA) coating, spatially confined pyrolysis under NH₃, acid etching, and thermal annealing to synthesize atomically dispersed Fe–Ni dual atoms embedded within a nitrogen-doped carbon matrix (FeNi DACs), which exhibited an outstanding activity toward both ORR and OER. X-ray photoelectron spectroscopy (XPS) analysis showed that pyridinic N made the primary contribution to the formation of FeNi dual-atom sites, and X-ray absorption near-edge spectroscopy (XANES) measurements confirmed that Fe was more positively charged, as attested by the higher white-line intensity, as compared to the Ni-free counterpart, indicating an enhanced interaction between the heteronuclear Fe–Ni dual-atom moiety and the defective nitrogen-doped carbon matrix.

In these studies, the experimental methods and selection of the supporting substrate materials can influence the formation efficiency and specific coordination configurations of the metal atoms. Despite the progress, significant challenges remain. Notably, in most syntheses, the products entail not only

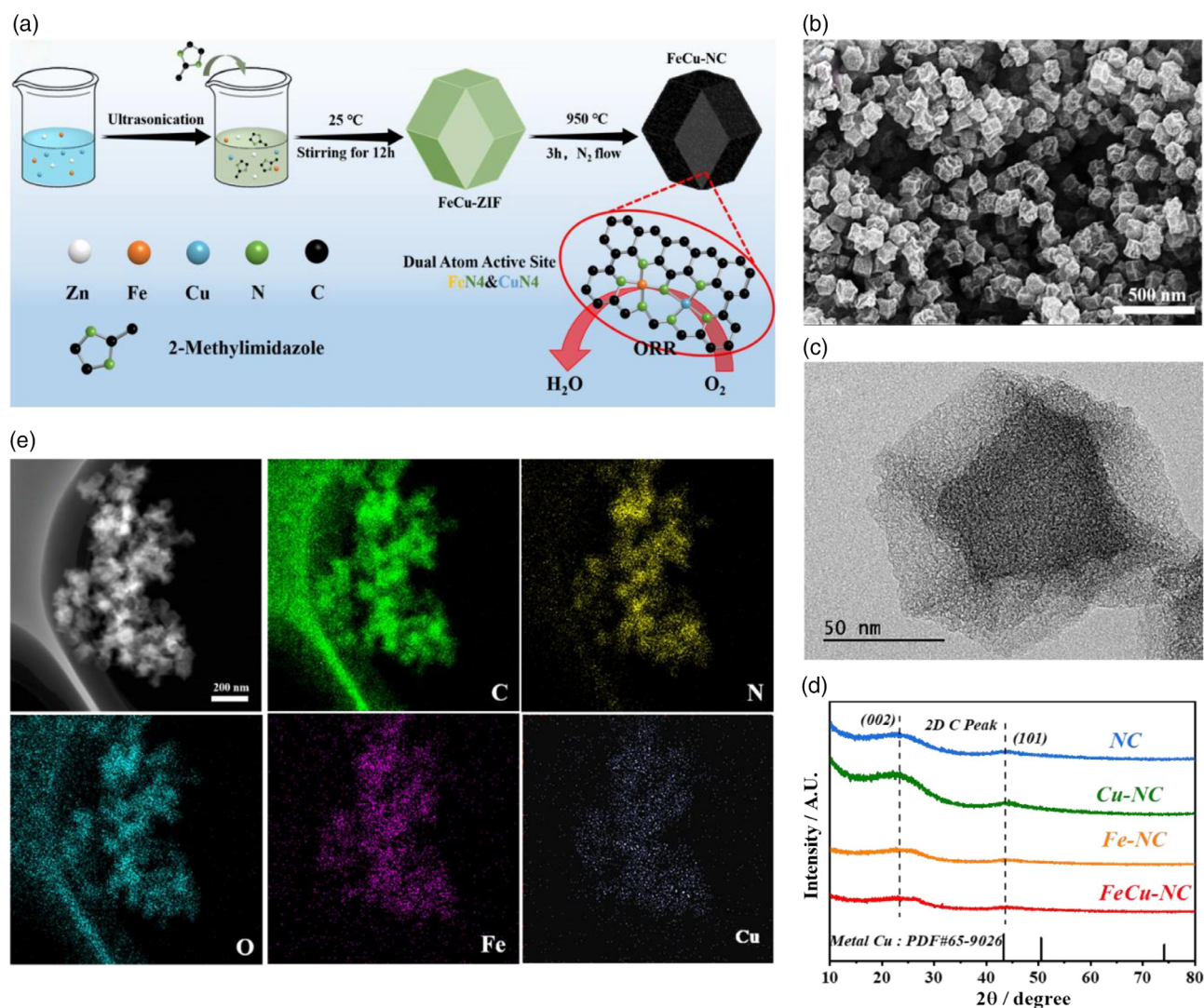


Figure 1. a) Schematic diagram of the synthesis of FeCu-NC nanocomposites. b) SEM and c) TEM images of FeCu-NC. d) X-ray diffraction (XRD) patterns of FeCu-NC, Fe-NC, Cu-NC, and NC. e) Elemental maps of FeCu-NC. Scale bars are b) 500 nm, c) 50 nm, and e) 200 nm. Adapted with permission.^[31] Copyright 2022, Elsevier B.V.

DACs, but also SACs. Such structural inhomogeneity renders it difficult to directly correlate the electrocatalytic activity with the materials structure. In addition, the synthetic procedures typically involve complex and harsh reaction conditions that limit the yield of DACs. Thus, further development of new, effective protocols is urgently needed.

2.2. Structural Characterization

Several unique experimental techniques play a critical role in the unambiguous determination of the dual-metal sites and their atomic configurations, beyond the conventional characterization tools, such as XPS and Raman spectroscopy. Among these, high-resolution transmission electron microscope (HRTEM) represents an indispensable tool in the structural characterization of DACs by not only visualizing the materials morphologies at

the nanoscale but also identifying the binuclear metal sites within the support matrix.^[35] The resolution can be markedly enhanced with aberration-corrected HRTEM (AC-HRTEM). For example, the Li group^[36] used AC-HRTEM to elucidate the formation of Co- and Fe-isolated atoms within a carbon support. HAADF-STEM is an even more powerful technique,^[37,38] which can directly visualize the atomic sites of the metal elements by taking advantage of the marked electronic density contrast against the carbon matrix. For instance, from the AC-HAADF-STEM images in **Figure 3**, one can clearly see the binuclear Co₂ atoms in panel (a) and Pt₂ in panel (b).

To directly probe the structural dynamics of DACs during the formation and electrochemical reactions, in situ transmission electron microscopy (TEM) has emerged as a unique tool. For instance, Zhu and co-workers^[39] employed in situ TEM to monitor the structural dynamics during electrochemical operation of Pt-Fe bimetallic nanocatalysts. From the evolution of

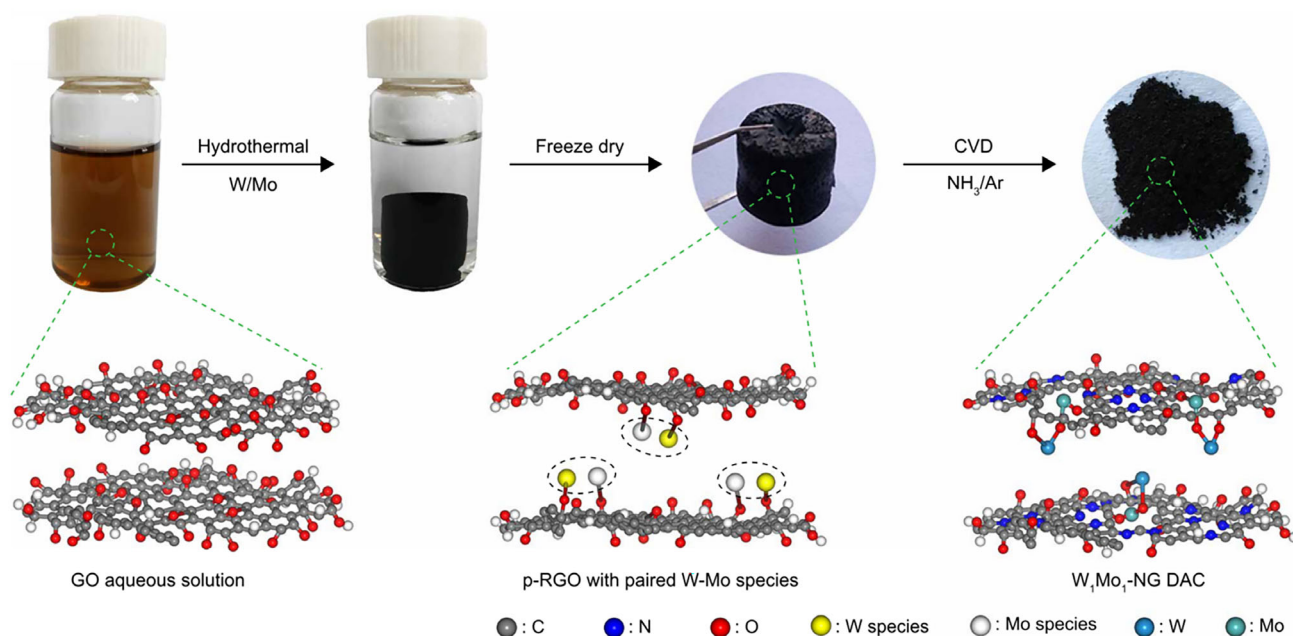


Figure 2. Schematic illustration of the synthetic procedure of W_1Mo_1 -N-doped graphene (NG) dual-atom catalysts (DACs). Reproduced from^[32] Copyright 2020, The Authors, some rights reserved; exclusive licensee AAAS. Distributed under a Creative Commons Attribution NonCommercial License 4.0 (CC BY-NC).

the diameter, number and composition of the metal clusters, the mechanism of bi-atomization for the formation of DACs was resolved, especially when the Kirkendall effect was involved.

In conjunction with TEM measurements that visualize the distributions of the metal atoms, elemental mapping analysis based on energy-dispersive X-ray spectroscopy (EDS) or electron energy loss spectroscopy (EELS) can be carried out to identify the chemical species of the metal elements, where EELS mapping is more elaborate than EDS, by taking advantage of their electron intensity difference.^[40] For example, Xing et al.^[41] used EELS mapping to confirm that Co atoms were in the proximity of N atoms, and in the Li group's work,^[36] the generation of Fe-Co binuclear sites within a carbon scaffold was attested by EELS mapping (Figure 3c).

Complementary structural insights can be obtained from X-ray spectroscopy measurements, in particular, to resolve the atomic configuration of the dual-metal centers of DACs. Among these, XAS has been attracting particular attention, which entails two techniques, XANES and EXAFS (extended X-ray absorption fine structure), that can shed lights on the metal valency as well as the coordination configuration within the supporting matrix. For instance, the Li group^[36] carried out XAS studies to unravel the structural details of nitrogen-doped carbon-supported FeCo DACs ((Fe,Co)/N-C), in comparison to iron (II) phthalocyanine (FePc) (Figure 4a). From the Fourier-transform (FT) profiles of EXAFS, it was found that (Fe,Co)/N-C mainly comprised the Fe-N coordination path (Figure 4b), and such path assignments can be aided by Wavelet transformation (WT) of EXAFS by correlating the R and k space profiles.^[42] In another study, Xiao et al.^[41] used WT-EXAFS to analyze the structure of a Co_2 DAC (Figure 4c). As compared to the Co-Co bond in Co nanoparticles, the Co-Co distance in the Co_2 DAC was shortened

with lower k and R values at the B site ($k = 6.88 \text{ \AA}^{-1}$) than at the C site ($k = 7.09 \text{ \AA}^{-1}$), consistent with the formation of Co-Co binuclear sites.

Another unique characterization tool is Mössbauer spectroscopy, which is a sensitive technique to characterize the spin properties of select metal centers, such as Fe and Sn, as magnetic moment of the metal centers has been found to impact the interactions with key reaction intermediates and hence the eventual electrocatalytic performance.^[11] For instance, Wang et al.^[36] carried out Mössbauer spectroscopy measurements to obtain structural insights into the coordination configurations of the active sites of Fe-Co DAC embedded within N-doped carbon. The appearance of the D1, D2, and D3 doublets suggested the formation of three types of square-planar $Fe^{II}N_4$ moieties in the sample in the high-, low-, and medium-spin states, respectively, and the occurrence of a minor singlet component of the iron species was due to the formation of the Fe-Co bond. In another study,^[43] the structures of Fe species in the Fe-Fe and Fe-Cu DACs were probed by ^{57}Fe Mössbauer spectroscopy measurements. Whereas the D1 and D2 doublets were observed in both Fe-Fe and Fe-Cu DACs, the fraction of the D2 component was markedly higher in Fe-Cu DAC than in Fe-Fe DAC, suggesting a decrease of the Fe spin state after Cu doping, in good accord with the variation of the magnetic moment evaluated by theoretical calculations.

To summarize, in comparison to SACs, the dual-metal atom structure of DACs calls for more sophisticated characterizations. In general, a combination of these complementary techniques is needed to clearly unravel the sample structure. This is needed in the construction of relevant structural models in theoretical simulations, and in the correlation with the electrochemical performance.

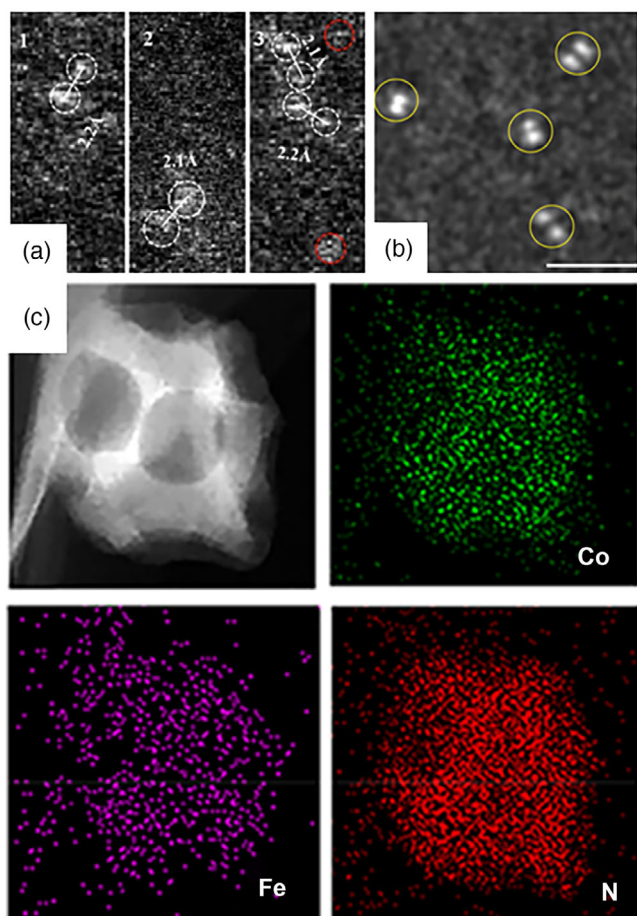


Figure 3. a) Aberration-corrected high-angle annular dark-field scanning transmission electron microscopy (HAADF-STEM) images of Co_2 nuclear sites in Co-C-N-10 (highlighted with white circles). Adapted with permission.^[41] Copyright 2018, Elsevier Ltd. b) Aberration-corrected HAADF-STEM image of Pt_2 dimers (highlighted with yellow circles). Scale bars 1 nm. Reproduced with permission under the terms of the Creative Commons CC BY license.^[18] Copyright 2017, the Authors. Published by Springer Nature. c) The corresponding electron energy loss spectroscopy (EELS) maps of Co, Fe, and N. Adapted with permission.^[36] Copyright 2017, American Chemical Society.

3. Electrocatalytic Performances

A wide variety of DACs has been developed in recent years and exhibited remarkable performances toward a range of key electrochemical reactions, such as HER, ORR, OER, CO_2RR , NRR , etc. In DACs, in particular, heteronuclear DACs, the two metal atoms can interact synergistically with each other, which enables the effective manipulation of the d-band center and optimizes the interaction of reaction intermediates with the catalytically active sites. The recent advancements of the design and engineering of DACs in these electrochemical reactions will be summarized in this section.

3.1. Hydrogen Evolution Reaction

Electrochemical water splitting is an important sustainable energy technology, which entails two half reactions, HER at

the cathode and OER at the anode, both of which necessitate the development of effective catalysts to overcome the high intrinsic energy barriers.^[44–46] Currently, Pt-based nanomaterials are the catalysts of choice for HER, $2\text{H}^+ + 2\text{e}^- \rightarrow \text{H}_2$. However, the high-cost and limited natural abundance have severely limited the widespread applications. Precious metal-free DACs have emerged as viable alternatives.^[47–50] In 2017, Kuang et al.^[51] developed a pyrolysis method to synthesize a CuCo@NC DAC with Cu and Co dual atoms embedded into a N-doped carbon framework. Experimentally, ZIF-67 was grown on the surface of $\text{Cu}(\text{OH})_2$ nanowires via an in situ process, followed by pyrolysis at 800°C . The prepared CuCo@NC DAC displayed a large surface area and an enhanced nitrogen doping efficiency due to the introduction of the atomically distributed Cu species. The CuCo@NC DAC exhibited an apparent HER activity in $0.5\text{ M H}_2\text{SO}_4$, needing a low overpotential ($\eta_{\text{HER},10}$) of -145 mV to reach the current density of 10 mA cm^{-2} , along with a small Tafel slope of 79 mV dec^{-1} , in comparison to Co@NC SAC ($\eta_{\text{HER},10} = -380\text{ mV}$, and Tafel slope 134 mV dec^{-1}). Zhou et al.^[52] synthesized a Fe-Rh DAC where Fe-Rh dual atoms were embedded into nitrogen-doped hollow carbon spheres. The resulting Fe-Rh DAC showed a high HER activity ($\eta_{\text{HER},10} = -36\text{ mV}$) and a low Tafel slope of 26 mV dec^{-1} . This was ascribed to the synergetic effect between Fe and Rh, where the Fe atom exhibited an enhanced charge density while the Rh site facilitated hydrogen adsorption and evolution, collectively enhancing the HER activity. Yang et al.^[32] prepared a DAC consisting of $\text{W}_1\text{Mo}_1\text{-NG}$. The distinctive W-O-Mo-O-C configuration was found to serve as the active site for HER, as the electron delocalization of the W-O-Mo-O-C configuration provided a desirable H-adsorption-free energy (ΔG_{H^*}) and boosted the HER kinetics. Indeed, the $\text{W}_1\text{Mo}_1\text{-NG}$ sample exhibited a remarkable HER performance in $0.5\text{ M H}_2\text{SO}_4$ with an overpotential ($\eta_{\text{HER},10} = -24\text{ mV}$) and Tafel slope (30 mV dec^{-1}) lower than those of $\text{Mo}_2\text{-NG}$ ($\eta_{\text{HER},10} = -145\text{ mV}$, Tafel slope 175 mV dec^{-1}), $\text{W}_2\text{-NG}$ ($\eta_{\text{HER},10} = -156\text{ mV}$, Tafel slope 107 mV dec^{-1}), and NG ($\eta_{\text{HER},10} = -200\text{ mV}$, Tafel slope 173 mV dec^{-1}).

Zhang et al.^[21] synthesized a Pt-Ru DAC by ALD deposition of Pt-Ru dimers on NCNTs (Figure 5a). The successful formation of the dimer-like structure was confirmed by HAADF-STEM measurements (Figure 5b–d). From the HER polarization curves in $0.5\text{ M H}_2\text{SO}_4$ at room temperature (Figure 5e), the Pt-Ru DAC can be seen to exhibit a markedly better activity than Pt SAC and commercial Pt/C. Specifically, the Pt-Ru DAC showed a current density of 23.1 A mg^{-1} at the overpotential of -50 mV , 54 times higher than that with Pt/C (Figure 5f), along with better stability (Figure 5g,h). Mechanistically, the synergetic effect between Pt and Ru rendered the d_{xz} orbital of Ru unoccupied, which weakened the interaction with H and enabled a high performance of the Pt-Ru DAC for HER.

In summary, DACs can indeed serve as high-performance catalysts toward HER due to their special structure and synergetic effects between the bimetal centers. Of particular notice is the development of DACs based on earth-abundant metals, such as Fe, Co, and Cu, such that the costs of the materials can be minimized. Table 1 lists the key results in recent studies of DACs for HER electrocatalysis.

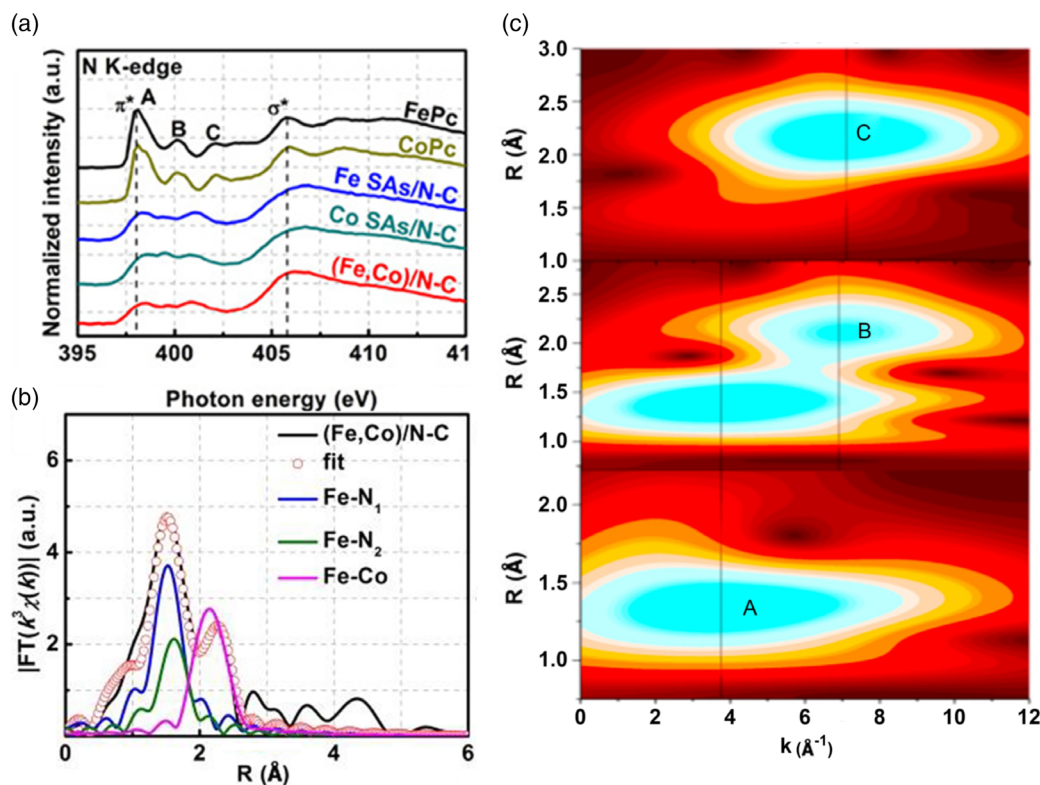


Figure 4. a) N K-edge X-ray absorption spectroscopy (XAS) spectra of Fe single atoms (SAs)/N-C, Co SAs/N-C, and (Fe,Co)/N-C. b) The corresponding Fe K-edge extended X-ray absorption fine structure (EXAFS) fittings of (Fe,Co)/N-C. Adapted with permission.^[36] Copyright 2017, American Chemical Society. c) Wavelet transformations (WTs) for the k^2 -weighted $\chi(k)$ Co K-edge EXAFS profiles. Adapted with permission.^[41] Copyright 2018, Elsevier Ltd.

3.2. Oxygen Evolution Reaction

As mentioned earlier, HER is the cathode reaction of electrochemical water splitting, and OER represents the anode reaction, $2\text{H}_2\text{O} \rightarrow \text{O}_2 + 4\text{H}^+ + 4\text{e}^-$, which is the reverse of ORR. Notably, a number of ORR electrocatalysts also show a remarkable performance for OER.^[53,54] For instance, the FeNi SAs/NC nanocomposites developed by Yu et al.^[34] were bifunctionally active toward both ORR and OER, displaying a low overpotential of ($\eta_{\text{OER},10} = +270$ mV) at 10 mA cm^{-2} for OER in 1.0 M KOH . DFT calculations showed that the energy barrier of the rate-determining step for OER was reduced by the synergetic interactions between the metal atoms and N-doped carbon matrix. Ma et al.^[55] prepared a Fe/Ni(1:3)-NG DAC, and observed an apparent activity for both ORR and OER ($\eta_{\text{OER},10} = +480$ mV) in 0.1 M KOH . The localization of the Fe $3d$ electrons was reduced by the introduction of the adjacent Ni sites, which improved the charge transfer at the interface and enhanced both ORR and OER activities. Bai et al.^[56] synthesized a Co-Fe DAC (Co-Fe-N-C), which exhibited a higher OER activity in alkaline electrolyte (1.0 M KOH) than Co-N-C (Figure 6a). The Co-Fe atom pairs were resolved by TEM and EDS measurements (Figure 6b-e). XAS measurements showed that the structure of Co-N-C changed upon immersion into an alkaline electrolyte, and Fe was then incorporated forming a dimeric Co-Fe moiety through one or two bridging OH groups after electrochemical activation. The

resulting Co-Fe-N-C composite exhibited a high OER activity with an $\eta_{\text{OER},10}$ of +321 mV, Tafel slope of 40 mV dec^{-1} , and a turnover frequency (TOF) of $\approx 1\text{ s}^{-1}$ at $\eta = +300$ mV and $\approx 12\text{ s}^{-1}$ at $\eta = +350$ mV (Figure 6f). These results suggested that Co-Fe-N-C could serve as a molecularly defined, nonprecious catalyst for OER. In another study,^[57] a Fe-Co DAC (meso/micro-FeCo-N_x-CN) with a well-defined 2D morphology was synthesized using silica nanoparticles as the templates. The sample featured a hierarchically meso- and microporous structure, and the homogenous dispersion of isolated metal atoms and very small metal clusters enabled the meso/micro-FeCo-N_x-CN to have reversible oxygen electrocatalytic sites, thus enhanced the electrocatalytic performance for both ORR and OER. For OER, $\eta_{\text{OER},10}$ was about +370 mV and the Tafel slope 57 mV dec^{-1} in 1.0 M KOH , lower than the comparative samples in the series. The meso/micro-FeCo-N_x-CN also exhibited impressive durability retaining more than 95% of the initial value after 10 h of operation and maintaining the potential of 1.7 V at 10 mA cm^{-2} .

Table 1 lists the OER performances of leading DACs in recent studies. One may note that Fe-Co DACs and Fe-Ni DACs are the most popular DAC choices for OER electrocatalysis, mostly because the Fe-Ni and Fe-Co configurations can enhance the electron transfer and lower the energy barrier of OER. In addition, the fact that Fe, Ni, and Co are low-cost, earth-abundant materials further renders them attractive options in further studies.

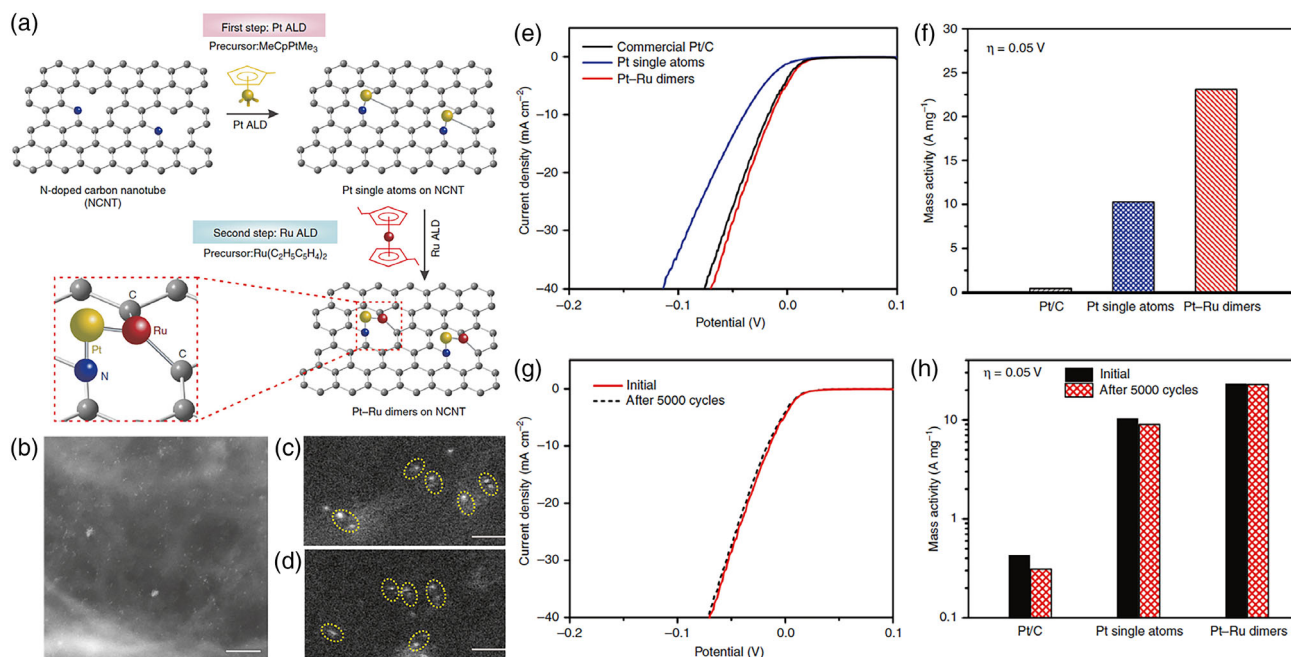


Figure 5. a) Schematic illustration of atomic layer deposition (ALD) synthesis of Pt–Ru dimers on nitrogen-doped carbon nanotubes (NCNTs). First, the Pt SAs were deposited by using MeCpPtMe₃ as the precursor. Then, the Pt–Ru dimers were prepared by selective deposition of Ru atoms on Pt SAs. Gray: C, blue: N, yellow: Pt, red: Ru. b–d) Aberration-corrected HAADF-STEM images of Pt–Ru dimers/NCNTs. Scale bars are b) 5 nm and c,d) 1 nm. The slowly varying contrast is due to the changes in the thickness of the substrate. e–h) Electrocatalytic performance of Pt–Ru dimers toward hydrogen evolution reaction (HER). e) HER polarization curves recorded on Pt–Ru dimers, Pt SAs and Pt/C catalysts. f) Normalized mass activity at –0.05 V of Pt–Ru dimers, Pt SAs, and Pt/C catalysts. g) Durability measurements of the Pt–Ru dimers catalysts. h) Normalized mass activity at –0.05 V of Pt–Ru dimers, Pt SAs, and Pt/C catalysts before and after durability tests. The Pt mass loadings for Pt/C, Pt SAs, and Pt–Ru dimers are 61.2, 1.34, and 1.24 μg cm^{–2}, respectively. Reproduced with permission under the terms of the Creative Commons CC BY license.^[21] Copyright 2019, the Authors. Published by Springer Nature.

3.3. Oxygen Reduction Reaction

ORR is a critical reaction at the cathode of metal–air batteries and fuel cells, $O_2 + 4H^+ + 4e^- \rightarrow 2H_2O$ in acid and $O_2 + 2H_2O + 4e^- \rightarrow 4OH^-$ in base.^[58–61] Due to the complex reaction pathways and sluggish electron-transfer kinetics, appropriate electrode catalysts are needed to drive the reaction such that a sufficiently high current density can be produced. Again, platinum-based nanomaterials have been used extensively as the leading catalysts.^[62] Developing low-cost, high-performance alternatives has been gaining increasing attention. For example, Xiao et al.^[41] pyrolytically synthesized a Co₂N₅ DAC and observed an enhanced ORR performance in 0.1 M HClO₄. STEM measurements confirmed the formation of binuclear Co–Co sites, and XAS measurements showed that the Co–Co path was 2.12 Å, deviating from the conventional CoN₄ moiety (1.90 Å) and Co nanoparticles (2.50 Å), which implied the formation of a special Co–Co path of the bimetallic atoms structure (Co₂N_x). Indeed, DFT calculations suggested the formation of Co₂N₅ sites. The ORR activity was found to be approximately 12 times higher than that of the conventional CoN₄ site in acidic media with a half-wave potential ($E_{1/2}$) of +0.79 V, which was the best among the Co–N–C catalysts and only 100 mV lower than that of commercial Pt/C. In another study,^[31] nanocomposites with Fe and Cu atomically dispersed into nitrogen-doped carbon with FeN₄ and CuN₄ dual-active sites (FeCu–NC DACs) were found to exhibit an

remarkable performance toward ORR in alkaline media, with an $E_{1/2}$ of +0.882 V, nearly 40 mV better than that of commercial Pt/C and 24 mV better than that of Cu-free Fe–NC SAC. This was ascribed to the strain caused by the CuN₄ moiety that replaced the carbon adjacent to FeN₄, which effectively tailored the electronic structure, weakened the OH* adsorption on FeN₄, and ultimately improved the catalytic activity.

The remarkably activity of Fe,Cu DACs was also demonstrated by He et al.^[43] where they reported a heteronuclear DAC with single-Cu sites incorporated into Fe–N–C aerogels (NCAG/Fe–Cu), and observed a remarkable ORR activity within a wide pH range of 0–14. Experimentally, the NCAG/Fe–Cu DACs were synthesized by a controlled pyrolysis process and followed by hydrofluoric acid (HF) etching (Figure 7a). The dual-atom structure was confirmed by the combined results of scanning electron microscopy (SEM) measurements, TEM measurements, and elemental mapping based on EDS and EELS (Figure 7b–e). In addition, in XPS measurements, the metal contents were estimated to be 0.92 wt% for NCAG/Fe–Fe and 0.94 wt% for NCAG/Fe–Cu (0.66 wt% Fe and 0.28 wt% Cu), suggesting that part of the Fe sites in the former were displaced by Cu. Furthermore, the atomic ratio between N in metal N and the total metal content was found to be close to 4:1, suggesting that MN₄ moieties were the dominant configuration in these carbon aerogels–supported DACs, in good agreement with results from XANES and EXAFS measurements, which confirmed the successful formation of

Table 1. Summary of electrochemical HER and OER performances of DACs in recent studies.

Catalyst	Reaction	η_{10} [mV]	Tafel Slope [mV dec ⁻¹]	Electrolyte	References
CuCo@NC	HER	-145	79	0.5 M H ₂ SO ₄	[51]
W ₁ Mo ₁ -NG	HER	-24	30	0.5 M H ₂ SO ₄	[32]
W ₁ Mo ₁ -NG	HER	-8	20	1.0 M KOH	[32]
FeRh-NCS	HER	-36	26	0.5 M H ₂ SO ₄	[52]
Cu/Ru@G _N	HER	-10	25	0.5 M H ₂ SO ₄	[48]
Cu/Ru@G _N	HER	-8	20	1.0 M KOH	[48]
Co-MoS ₂ /BCCF-21	HER	-48	52	1.0 M KOH	[47]
Pt ₁ @ Fe-N-C	HER	-60	42	0.5 M H ₂ SO ₄	[53]
Pt-Ru dimer	HER	-50	28.9	0.5 M H ₂ SO ₄	[21]
FeNi SAs/NC	OER	+270	54.68	1.0 M KOH	[34]
Fe/Ni(1:3)-NG	OER	+480		0.1 M KOH	[55]
Co-Fe-N-C	OER	+321	40	1.0 M KOH	[56]
FeCo-NC	OER	+349	99.93	0.1 M KOH	[24]
meso/micro-FeCo-N _x -CN	OER	+370	57	1.0 M KOH	[57]
FeMn-DSAC	OER	+405	96	0.1 M KOH	[54]
Co ₁ -PNC/Ni ₁ -PNC	OER	+390	117	1.0 M KOH	[25]
NiFe@PCN	OER	+310	38	1.0 M KOH	[26]
Pt ₁ @ Fe-N-C	OER	+310	62	0.1 M KOH	[53]

FeN₄ and CuN₄ sites in the NCAG/Fe-Cu sample. In electron paramagnetic resonance measurements, the Fe spin state in NCAG/Fe-Cu was found to decrease, as compared to that of NCAG/Fe-Fe, due to electronic modulation by the adjacent Cu atoms. First principles calculations indeed showed that the neighboring metal sites could manipulate the Fe spin state in FeN₄ through the 3d electrons, which showed an obvious influence on the ORR catalytic activity. Electrochemically, NCAG/Fe-Cu exhibited an excellent ORR activity, with a high $E_{1/2}$ of +0.94 V in alkaline media (Figure 7g,h), +0.84 V in neutral media (Figure 7j,k), and +0.78 V in acidic media (Figure 7i). In addition, the NCAG/Fe-Cu exhibited high stability, where the peak potential of oxygen reduction shifted negatively by only 13 mV after 8000 cycles in 1.0 M phosphate-buffered saline (PBS), much lower than that (27 mV) with NCAG/Fe-Fe (Figure 7l).

One may notice that in these two FeCu DACs,^[31,43] the NCAG/Fe-Cu sample exhibited a somewhat better ORR performance in 0.1 M KOH than FeCu-NC with a higher onset potential (E_{onset} , +1.07 vs +0.96 V), $E_{1/2}$ (+0.94 vs +0.882 V) and lower Tafel slope (55 vs 74 mV dec⁻¹), despite the formation of a similar FeN₄-CuN₄ moiety. Such a discrepancy may be, at least in part, ascribed to the different morphology of the carbon scaffold,

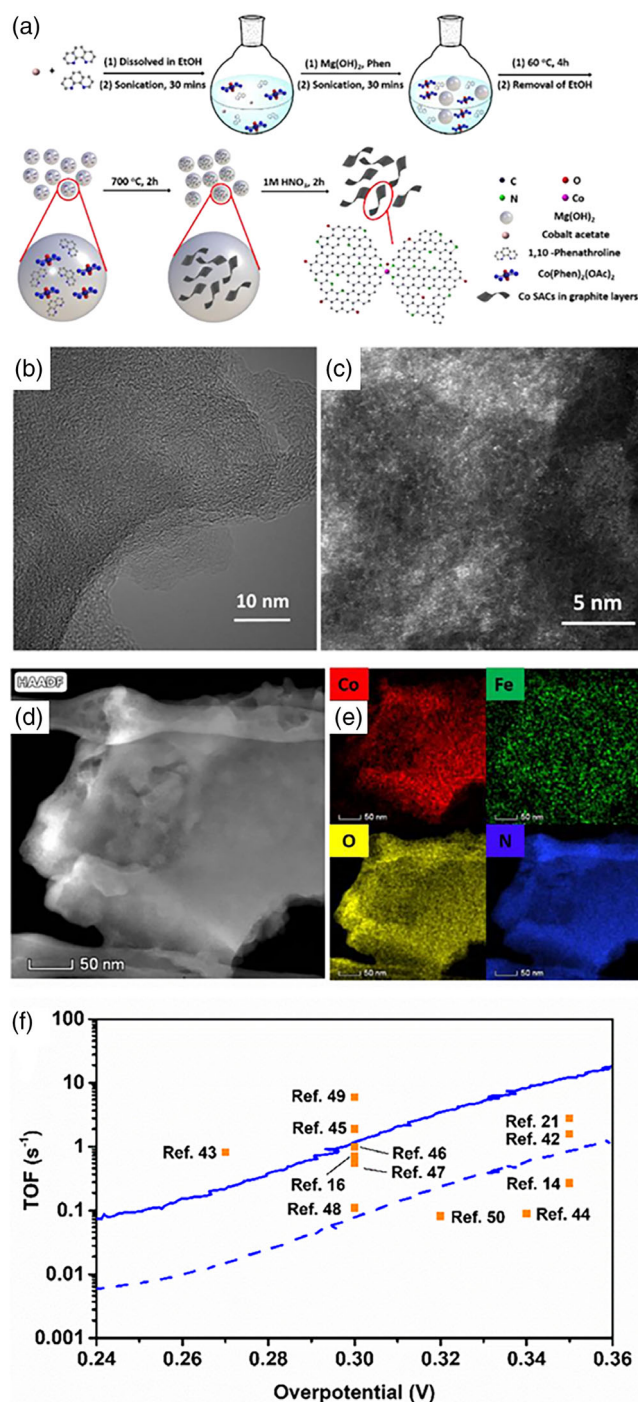


Figure 6. a) Synthesis of Co-N-C, b) high-resolution TEM (HRTEM), and c) spherical aberration-corrected HAADF-STEM images of Co-N-C after activation in Fe-containing KOH (Co-Fe-N-C). d) HAADF-STEM image of Co-Fe-N-C and e) the corresponding EDS-based elemental mapping of panel (c). f) Potential-dependent turnover frequencies (TOFs) of Co-Fe-N-C (solid line) and all-metal-based TOFs (dashed line) in comparison with selected state-of-the-art catalysts. Scale bars are b) 10 nm, c) 5 nm, d) 50 nm, and e) 50 nm. Adapted with permission.^[56] Copyright 2019, American Chemical Society.

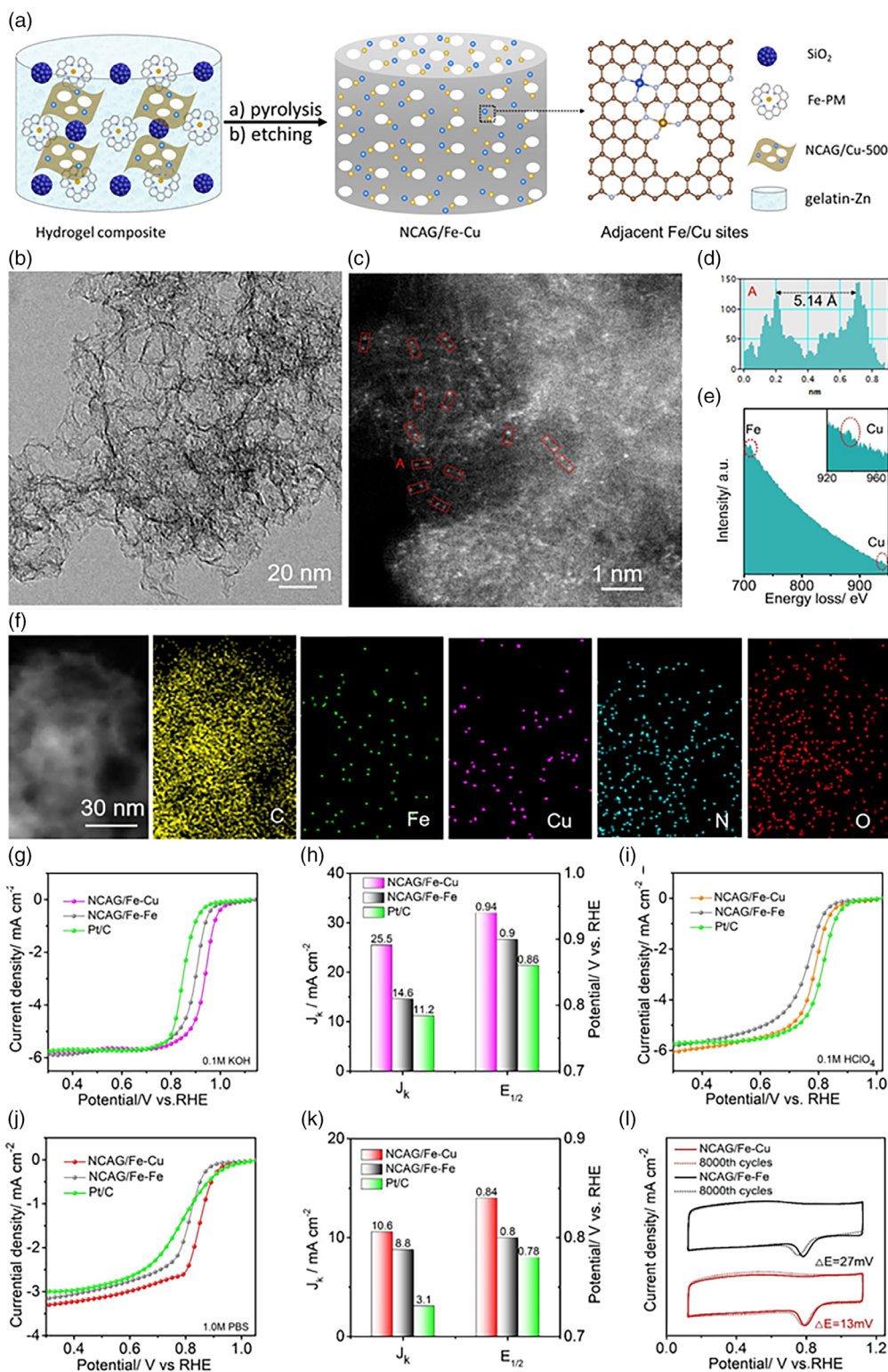


Figure 7. a) Schematic illustration of the preparation of NCAG/Fe–Cu carbon aerogels. b) TEM and c) STEM images of NCAG/Fe–Cu. d) The intensity profile and e) EELS spectrum of the red box A in (c). Inset to (e) is the zoom in of the Cu signal. f) TEM image and the corresponding elemental maps of NCAG/Fe–Cu. g) Linear sweep voltammetry (LSV) curves, and h) J_k (at +0.85 V) and $E_{1/2}$ of NCAG/Fe–Cu, NCAG/Fe–Fe and commercial Pt/C in 0.1 M KOH. i) LSV curves of NCAG/Fe–Cu, NCAG/Fe–Fe, and commercial Pt/C in 0.1 M HClO₄. j) LSV curves, and k) J_k (at 0.85 V) and $E_{1/2}$ of NCAG/Fe–Cu, NCAG/Fe–Fe and commercial Pt/C in 1.0 M phosphate-buffered saline (PBS). l) Cyclic voltammetry (CV) curves of durability tests in 1.0 M PBS. Scale bars are b) 20 nm, c) 1 nm, and f) 30 nm. Adapted with permission.^[43] Copyright 2022, Wiley-VCH.

where the nanowrinkled carbon aerogels in NCAG/Fe–Cu were known to further impact the electronic distribution of the metal active sites and facilitated the adsorption of oxygen intermediates.^[43]

Wang et al.^[36] synthesized FeCo/NC DACs by a host–guest design strategy with porphyrin-like Fe–Co dual sites occupying the confined space of a metal–organic framework (MOF) by controlling the bonding interactions between the Co nodes (host) and adsorbed Fe ions (guest). Compared to commercial Pt/C, the FeCo/NC DACs exhibited an enhanced ORR performance in 0.1 M HClO₄ with a higher E_{onset} (+1.06 vs +1.03 V) and $E_{1/2}$ (+0.863 vs +0.858 V). In rotating disk electrode tests, the FeCo/NC DACs exhibited long-term stability even after more than 5000 cycles and tolerance to carbon monoxide and methanol. The high activity and selectivity to the 4e[−] ORR were ascribed to the unique configuration of the Fe–Co dual-atom site that favored the activation and cleavage of the O–O bond, as confirmed by DFT calculations. Zhang et al.^[63] also prepared a Pt–Co DAC supported on nitrogen-doped carbon (A–CoPt–NC) and observed a high selectivity for the 4e[−] pathway in ORR in 0.1 M KOH, with a high $E_{1/2}$ of +0.96 V, 90 mV higher than that of commercial Pt/C. A–CoPt–NC also exhibited better stability, retaining 96.4% of the initial current density after 4 h of reaction, as compared to 79.7% for Pt/C. DFT calculations showed that the high ORR activity was due to the synergetic effect of the Pt–Co dual-atom sites located on a defected C/N graphene surface and the asymmetrical distribution of the electrons around the Pt/Co centers.

Samireddi et al.^[64] prepared DACs that combined Co and Fe with a corrole–N₄ center (PhFCC). The PhFCC exhibited a remarkable ORR performance within a wide range of pH, with an E_{onset} of +0.86 V and $E_{1/2}$ of +0.75 V in acidic media, and +0.94 and +0.85 V in alkaline media. The PhFCC also showed impressive durability with a negative shift of $E_{1/2}$ by only 25 mV in acidic media and 5 mV in alkaline media after 3000 potential cycles. Yu et al.^[34] developed atomically dispersed Fe–Ni DACs embedded in a nitrogen-doped carbon matrix (FeNi/NC), which showed an impressive ORR performance with a high E_{onset} of +0.98 V and $E_{1/2}$ of +0.84 V in 0.1 M KOH. DFT calculations showed that the Fe sites acted as the active centers in the 4e[−] pathway, and the electronic structure of Fe sites was regulated by the adjacent Ni sites, which reduced the energy barrier of the rate-determining step. Ma et al.^[53] prepared DACs with atomically dispersed FeN₄ and NiN₄ in nitrogen-doped graphene (FeNi–NG), and observed a high ORR activity in 0.1 M KOH, with $E_{1/2}$ = +0.842 V. Chen et al.^[65] prepared Fe₁Se₁–NC DACs which displayed a markedly higher ORR activity than Fe₁–NC and Se₁–NC. DFT calculations and spectroscopic characterizations showed that the introduction of neighboring Se sites led to the generation of new active sites, and tuned the charge redistribution and spin state of the Fe sites. Moreover, the desorption of *OH, which was the rate-determining step, was also facilitated by the coexistence of FeN₅ and SeC₂ dual active sites. Mercado et al.^[66] synthesized a DAC with Fe and Co dual-metal atoms embedded into nitrogen-doped porous carbon cages (CHS–FeCo) by controlled pyrolysis of silica nanoparticle–supported melamine–formaldehyde resin embedded with iron and cobalt precursors, followed by acid etching. The CHS–FeCo exhibited an impressive ORR performance with E_{onset} = +0.93 V and $E_{1/2}$ = +0.79 V. Repeated potential sweeping showed that the polarization curves of CHS–FeCo remained virtually unchanged

for up to 10 000 cycles, due to the strong incorporation of the metal centers into the carbon skeletons.

Table 2 lists the ORR performances of leading DACs in recent studies, in comparison with commercial Pt/C. One can see that DACs can indeed serve as effective catalysts toward ORR due to the synergetic effects between the bimetal sites which reduce the energy barrier in the four-electron pathway of ORR.

3.4. Metal–Air Battery

Rechargeable metal–air batteries have attracted a great deal of attention due to their low cost and high energy density.^[57,67–70] Development of bifunctional ORR/OER catalysts represents a critical initial step. DACs have emerged as unique viable candidates where the two metal centers may be responsible for the two reactions, and the metal–metal interactions may be exploited for the enhanced performance as compared to their monometallic SAC forms. For instance, Cui et al.^[54] prepared a FeMn–DSAC composite which consisted of adjacent FeN₄ and MnN₄ sites on 2D ultrathin porous N-doped carbon nanosheets. FeMn–DSAC exhibited an impressive activity toward both ORR and OER, featuring a narrow potential gap ($\Delta E = 0.713$ V) between the ORR half-wave potential ($E_{1/2}$) and OER potential ($E_{\text{OER},10}$) at 10 mA cm^{−2} in 0.1 M KOH and could be used as the cathode catalyst for a flexible low-temperature zinc–air battery (ZAB). The FeMn–DSAC-based ZAB showed a peak power density of 30 mW cm^{−2} and retained up to 86% of the specific capacity from room temperature to −40 °C. DFT calculations revealed that the synergistic effect between the Fe–Mn dual sites and the porous 2D nanosheet structure enhanced *OOH dissociation and hence the remarkable ZAB performance.

Wu et al.^[71] synthesized a 3D porous Fe–Co DSAC (FeCo–NSC) via a soft template-directed interlayer confinement route (Figure 8a), which consisted of FeN₄S₁/CoN₄S₁ coordination moieties embedded in 2D carbon nanosheets. Such morphological characteristics were revealed in SEM and TEM measurements (Figure 8b,c); and STEM measurements, along with elemental mapping, clearly showed the homogeneous distributions of the C, N, S, Co, and Fe elements (Figure 8d). The FeCo–NSC could be used as the air cathode catalyst for a primary liquid ZAB (along with a Zn-plate anode) (Figure 8e), thanks to the remarkable bifunctional activity toward ORR and OER, with a high open-circuit potential (OCP) of 1.51 V (markedly higher than 1.45 V based on commercial Pt/C) (Figure 8f), a high specific capacity of 782.1 mA hg_{Zn}^{−1} at 20 mA cm^{−2} (95.3% of the theoretical capacity) (Figure 8h) and a maximum power density of 152.8 mW cm² at 252.1 mA cm² (in comparison to 116.3 mW cm² at 169.8 mA cm² for the Pt/C-based battery) (Figure 8i). The FeCo–NSC-based ZAB was also able to maintain a potential of 1.49 V after continuous operation for 6000 s, which was higher than those based on other comparative catalysts, such as Fe–NSC (1.44 V), Co–NSC (1.39 V), and commercial Pt/C (1.48 V), demonstrating the best durability among the series (Figure 8g). From the results of DFT calculations, it was found that the synergistic interactions between the Fe–Co dual-metal centers optimized the adsorption/desorption of oxygen reaction intermediates and decreased the energy barriers for enhanced ORR.

Table 2. Summary of the ORR performances of select DACs versus Commercial Pt/C.

Catalyst	E_{onset} (V vs. RHE)	$E_{1/2}$ (V vs. RHE)	Tafel Slope [mV dec ⁻¹]	n	Electrolyte	Loading [mg cm ⁻²]	References
NCAG/Fe–Cu	+1.07	+0.94	55	4	0.1 M KOH	0.425	[43]
FeCu–NC	+0.96	+0.882	74	3.97	0.1 M KOH	0.24	[31]
(Fe,Co)/N–C	+1.06	+0.863	66	4	0.1 M HClO ₄	0.77	[36]
A–CoPt–NC		+0.96		4	0.1 M KOH	0.262	[63]
PhFCC	+0.94	+0.85		3.94	0.1 M KOH	0.25	[64]
	+0.86	+0.75		3.96	0.1 M HClO ₄		
FeNi SAs/NC	+0.98	+0.84	54.68	4	0.1 M KOH	0.4	[34]
Fe/Ni(1:3)–NG		+0.842		3.8	0.1 M KOH		[55]
Fe ₁ Se ₁ –NC	+1.0	+0.88		4	0.1 M KOH		[65]
CHS–FeCo	+0.93	+0.79	86.1	3.6	0.1 M KOH	0.0813	[66]
CuCo@NC	+0.96	+0.884	80	3.78	0.1 M KOH	0.182	[51]
FeMn–DSAC	+1.04	+0.922	33	3.98–4	0.1 M KOH	0.30	[54]
Commercial Pt/C	+1.03	+0.858	68	4	0.1 M HClO ₄		[36]

The aforementioned NCAG/Fe–Cu nanocomposites by He et al.^[43] also exhibited an outstanding performance as bifunctional cathode catalysts in a neutral/quasi-solid aluminum–air and alkaline/quasi-solid zinc–air batteries. The NCAG/Fe–Cu//Al battery showed an OCP of 2.00 V and a peak power density of 137 mW cm⁻², which were about 200 mV and 41 mW cm⁻² higher those of a Pt/C//Al battery. The NCAG/Fe–Cu//Zn quasi-solid battery also exhibited a better OCP (1.51 vs 1.40 V) and maximum power density (186 vs 100 mW cm⁻²), along with excellent mechanical flexibility. These results highlight the unique potential of NCAG/Fe–Cu as viable bifunctional oxygen catalysts for metal–air batteries.

3.5. CO₂ Reduction Reaction

Electrochemical CO₂RR can not only reduce the atmospheric CO₂ concentration but also convert the chemically inert CO₂ into fuels and other value-added chemicals, a critical step in the carbon-neutral economy.^[72,73] However, the large-scale application of CO₂RR is severely hindered by the lack of efficient, selective, and stable electrocatalysts. Recently, DACs with two interacting metal atoms have been shown to be effective CO₂RR catalysts, due to the manipulation of the adsorption configuration of reactant molecules. Compared to SACs, the dual-atom sites allow both C and O atoms of CO₂ to adsorb onto the metal atoms, thus reducing the adsorption free energy of the intermediates and lowering the activation barrier caused by the stable C=O bonds in CO₂. For instance, Li et al.^[74] prepared a dual-atom Ag₂/graphene catalyst featuring well-defined AgN₃–AgN₃ active sites for CO₂RR. The Ag₂/graphene catalysts were synthesized by a high-temperature treatment method and could drive CO₂RR at a potential as high as –0.25 V, with an excellent CO Faraday efficiency (FE_{CO}) up to 93.4% and a current density of 11.87 mA cm⁻² at –0.7 V in 0.5 M KHCO₃ and long-term stability, far surpassing the SA Ag₁/graphene and the traditional silver nanoparticle catalysts. Mechanistically, the dual-atom Ag₂ sites lowered the barrier for the formation of *COOH by stabilizing the *CO₂ intermediate through the concomitant interactions

with the C and one of the O atoms of CO₂, as shown in DFT calculations. In another study, Zhang et al.^[75] synthesized carbon-supported Pd₂ DAC and observed that the electron transfer between the Pd atoms at the dimeric sites led to a moderate CO adsorption and facilitated CO production from CO₂RR, featuring a 98.2% FE_{CO} at +0.85 V that was much better than that of Pd₁ SAC, along with long-term stability.

In addition, Wang et al.^[76] prepared a Fe₂ DAC where the dual-iron sites were anchored on a nitrogen-doped carbon matrix (Fe₂–N–C). Compared to Fe SAC, the Fe₂ DAC showed better durability and an FE_{CO} above 80% in a wide potential range, along with a high TOF (26 637 h⁻¹) in 0.5 M KHCO₃. The synergistic effects of the Fe₂ sites overcame the disadvantages of SACs on the desorption of *CO intermediates and facilitated the CO₂-to-CO conversion. Cao et al.^[77] synthesized a Ni₂ DAC with a unique bridging structure of binuclear nickel atoms coordinated with four nitrogen and two carbon atoms (Ni₂–N₄–C₂, Ni–CNC-1000) by the electrospinning method and subsequent pyrolysis (Figure 9a). The coordination structure of the atomic nickel sites was unraveled by SEM, TEM, and EDS measurements (Figure 9b–g). The Ni–CNC-1000 exhibited a high FE_{CO} (96.6% at –0.8 V) (Figure 9h) and a remarkable TOF value (4606.5 h⁻¹ at –1.0 V) in 0.5 M KHCO₃ (Figure 9i) in an H-type cell, and an outstanding low onset potential (–0.2 V) and a maximal FE_{CO} (97.8% at –0.5 V) in a flow cell with an alkaline electrolyte (1 M KOH) (Figure 9j,k). In an assembled Zn–CO₂ cell, the Ni–CNC-1000 showed an impressive peak power density of 2.43 mW cm⁻² in the discharge process with excellent stability as the cathode catalyst. The unique bridging structure of binuclear Ni atoms with four nitrogen and two carbon atoms (Ni₂–N₄–C₂) led to the adjustment of the electronic structure of the d-states in Ni₂–N₄–C₂ for the optimal activation and adsorption of reaction intermediates, thus facilitating the activity and selectivity for CO₂RR, as confirmed in DFT calculations.

In another study, Zhang et al.^[75] prepared Pd₂ DACs by an anion-replacement deposition–precipitation method for CO₂RR. The Pd₂ DAC exhibited long-term stability and an excellent catalytic performance with a 98.2% FE_{CO} at –0.85 V in 0.5 M KHCO₃,

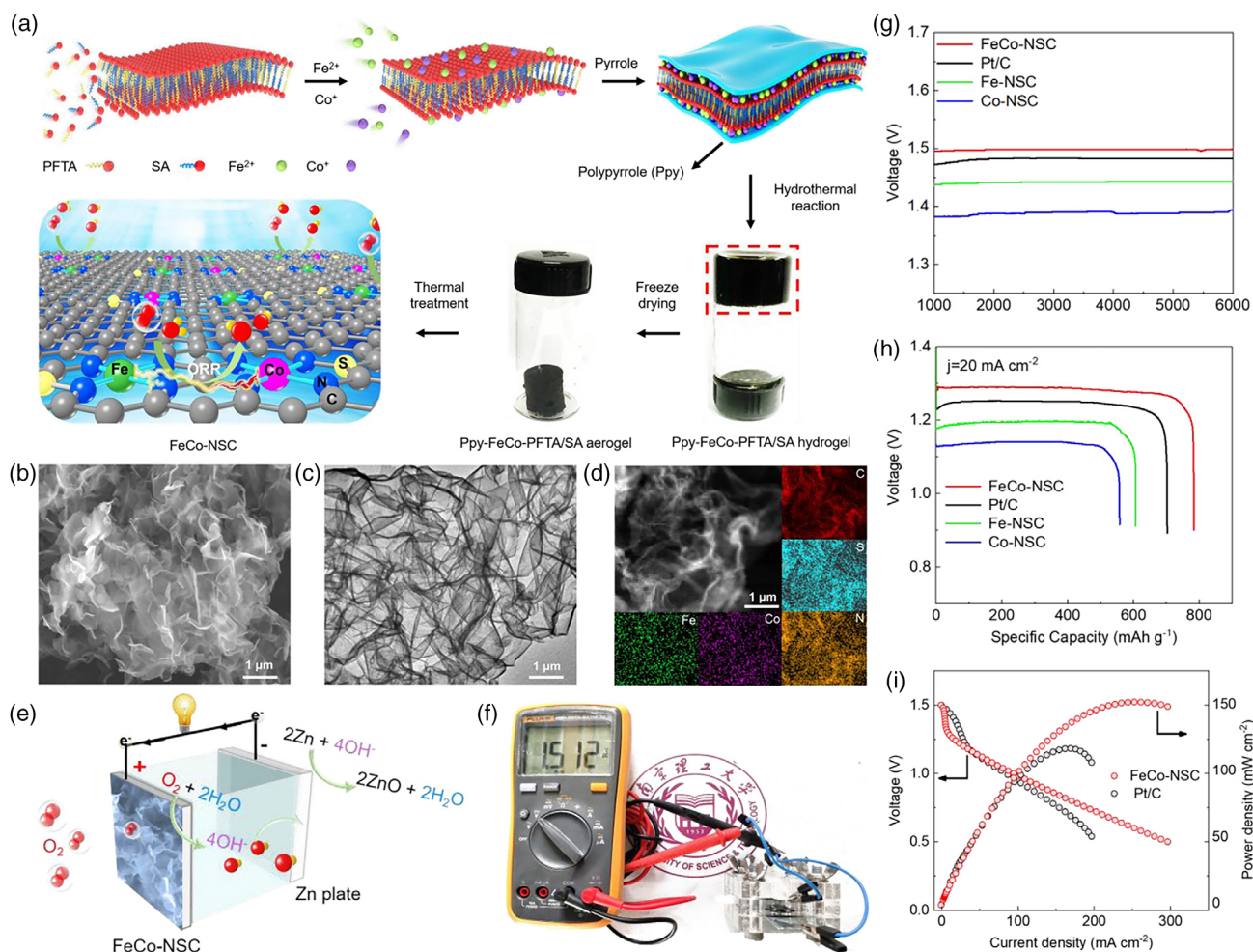


Figure 8. a) Schematic illustration of the synthesis procedure for the FeCo-NSC. b) SEM and c) TEM images of FeCo-NSC. d) HAADF-STEM image and the corresponding elemental mapping of FeCo-NSC. e) Illustration of a designed Zn–air battery with a FeCo-NSC cathode and Zn-plate anode. f) Photograph of a FeCo-NSC-based zinc–air battery (ZAB) showing an open-circuit voltage of 1.512 V. g) Open-circuit voltage curves and h) galvanostatic discharge curves of ZABs based on FeCo-NSC, Fe-NSC, Co-NSC, and Pt/C. i) Discharge polarization and the corresponding power density curves of ZABs based on FeCo-NSC and Pt/C. Scale bars in (b–d) are all 1 μm . Adapted with permission.^[71] Copyright 2021, Elsevier B.V.

far exceeding that of Pd₁ SAC. DFT calculations showed that Pd₂ was close to the top of the volcano plot with an optimized limiting potential (U_1) and the moderate adsorption strength of CO* was beneficial for CO production in CO₂RR. Xie et al.^[78] synthesized a NiSn atomic pair DAC (NiSn–APC) by an impregnation plus pyrolysis treatment (Figure 10a), where both Ni and Sn were coordinated with four nitrogen atoms (N₄Ni–SnN₄) (Figure 10b–e). The NiSn–APC exhibited a higher activity and selectivity than relevant electrocatalysts reported in the literature for CO₂RR to formate, with a TOF of 4752 h⁻¹ and formate productivity of 36.7 mol h⁻¹g_{sn}⁻¹ in 0.5 M KHCO₃ (Figure 10f). The NiSn–APC also displayed a higher-utilization efficiency (57.9%) of the active sites, as compared to the SAC counterparts (Figure 10g). DFT calculations showed that the Si site was the active site for CO₂RR to formate, and the synergistic interactions between the Sn and Ni sites reduced the energy barrier of the production of *OCHO intermediate, leading to an enhanced catalytic performance for CO₂RR to formate (Figure 10h,i).

Ren et al.^[79] reported the production of Ni/Fe–N–C DACs by an ion-exchange strategy followed by pyrolysis of a Zn/Ni/Fe-containing ZIF. The Ni/Fe–N–C DAC displayed a high catalytic activity toward CO₂RR in 0.5 M KHCO₃ with a higher current density (7.4 mA cm⁻² at -0.7 V), maximum FE_{CO} of 98% at -0.7 V and TOF (7682 h⁻¹ at -1.0 V) than Ni–N–C (4.9 mA cm⁻² at -0.7 V and 3690 h⁻¹ at -1.0 V) and Fe–N–C (1.6 mA cm⁻² at -0.7 V and 813 h⁻¹ at -1.0 V). After 30 h of continuous electrolysis, the Ni/Fe–N–C also retained 99% of the initial FE_{CO} (≈ 8 mA cm⁻²), indicating good durability for CO₂RR. The structural change of the bimetal–nitrogen sites reduced the energy barrier for both the formation of COOH* intermediate and the desorption of CO. Moreover, DFT calculations showed that the synergistic effect of the neighboring Ni–Fe centers decreased the reaction barrier for the formation of COOH* and desorption of CO, leading to a remarkable CO₂RR activity. In another study, Meng et al.^[80] synthesized a Bi–Zn DAC (BiZn/NC) by a gas-migration/NH₃-mediated strategy, which

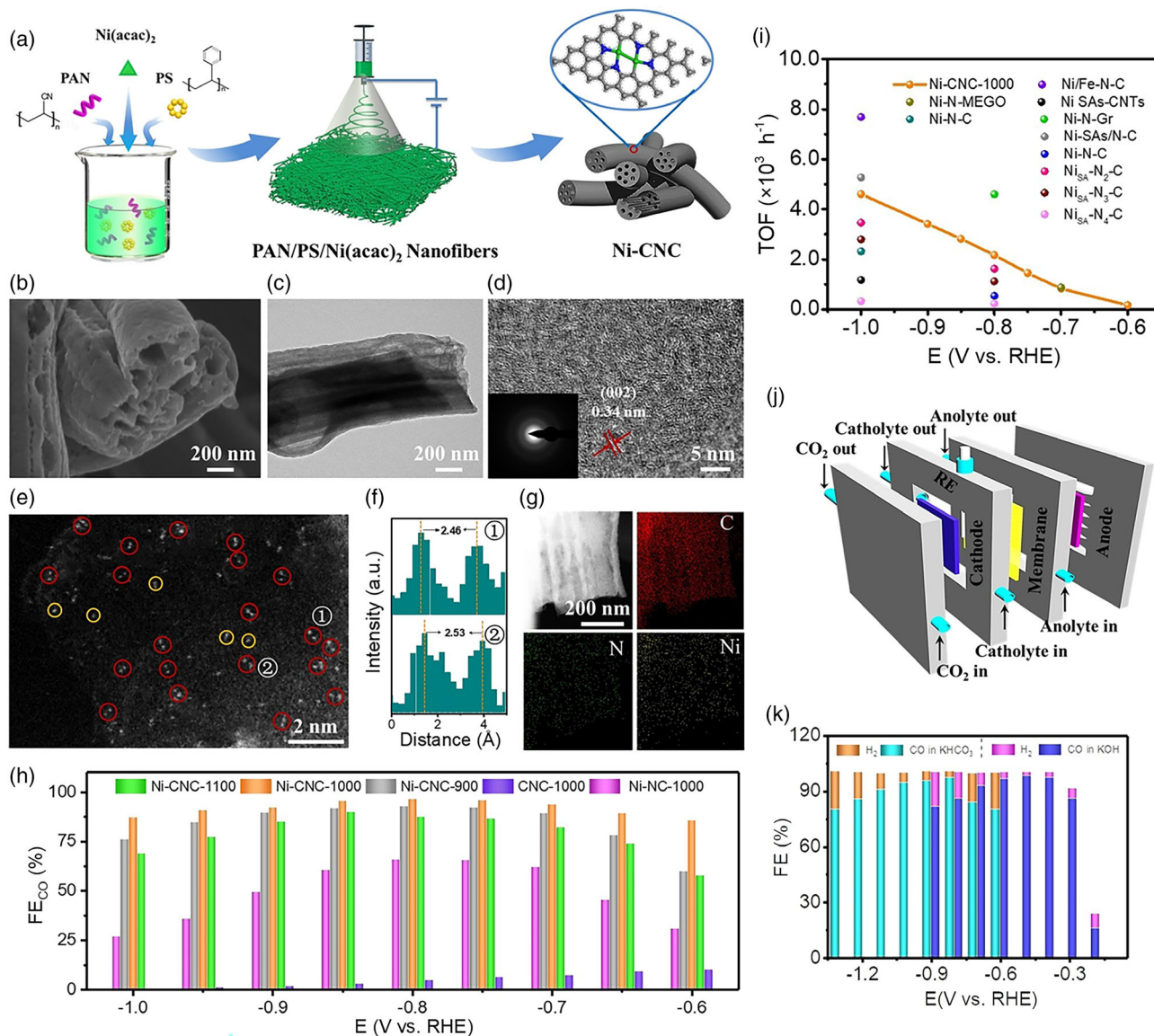


Figure 9. a) Illustration for the preparation of binuclear nickel atoms coordinated with four nitrogen and two carbon atoms (Ni₂-N₄-C₂, Ni-CNC) fibers via the electrospinning method followed by pyrolysis. b) SEM, c) TEM, d) HRTEM, e) HAADF-STEM images, and f) the corresponding intensity profiles of Ni-CNC-1000. g) Elemental maps of Ni-CNC-1000. h) FE_{CO} of the Ni-CNC-1000 electrode in 0.5 M KHCO₃ in an H-type cell. i) TOF of Ni-CNC-1000 compared with state-of-the-art CO₂-to-CO catalysts. j) Schematic illustration of the flow cell configuration. k) FE_{CO} of the Ni-CNC-1000 electrode in 1 M KHCO₃ or 1 M KOH in a flow cell. Scale bars are b) 200 nm, c) 200 nm, d) 5 nm, e) 2 nm, and g) 200 nm. Adapted with permission.^[77] Copyright 2021, Wiley-VCH.

enhanced the catalytic performance of the electrochemical conversion of CO₂ and H₂O to syngas. The pyridinic-N-Bi/Zn bonding moiety was argued to be key to the improvement of the electrocatalytic activity. Compared with other electrocatalysts used in syngas production by the Fischer-Tropsch process, BiZn/NC exhibited a more efficient performance to tune the CO/H₂ ratios within the range from 0.20 to 2.92.

In CO₂RR, a range of valuable products can be produced, such as CO, formic acid, alcohols, and hydrocarbons.^[78,81–83] However, most DACs reported thus far are limited to CO₂ reduction to CO, likely due to the limited number of active sites for the

concurrent adsorption of other intermediates required for the formation of more complicated products.^[15] Further structural engineering of the nanocomposite catalysts is therefore strongly desired to achieve both high activity and selectivity of CO₂RR.

3.6. Nitrogen Reduction Reaction

NRR is a green technology that can be used for the artificial fixation of nitrogen into ammonia, a commodity chemical used widely across the globe.^[84] However, the traditional nitrogen fixation (e.g., the Haber-Bosch process) is energy- and

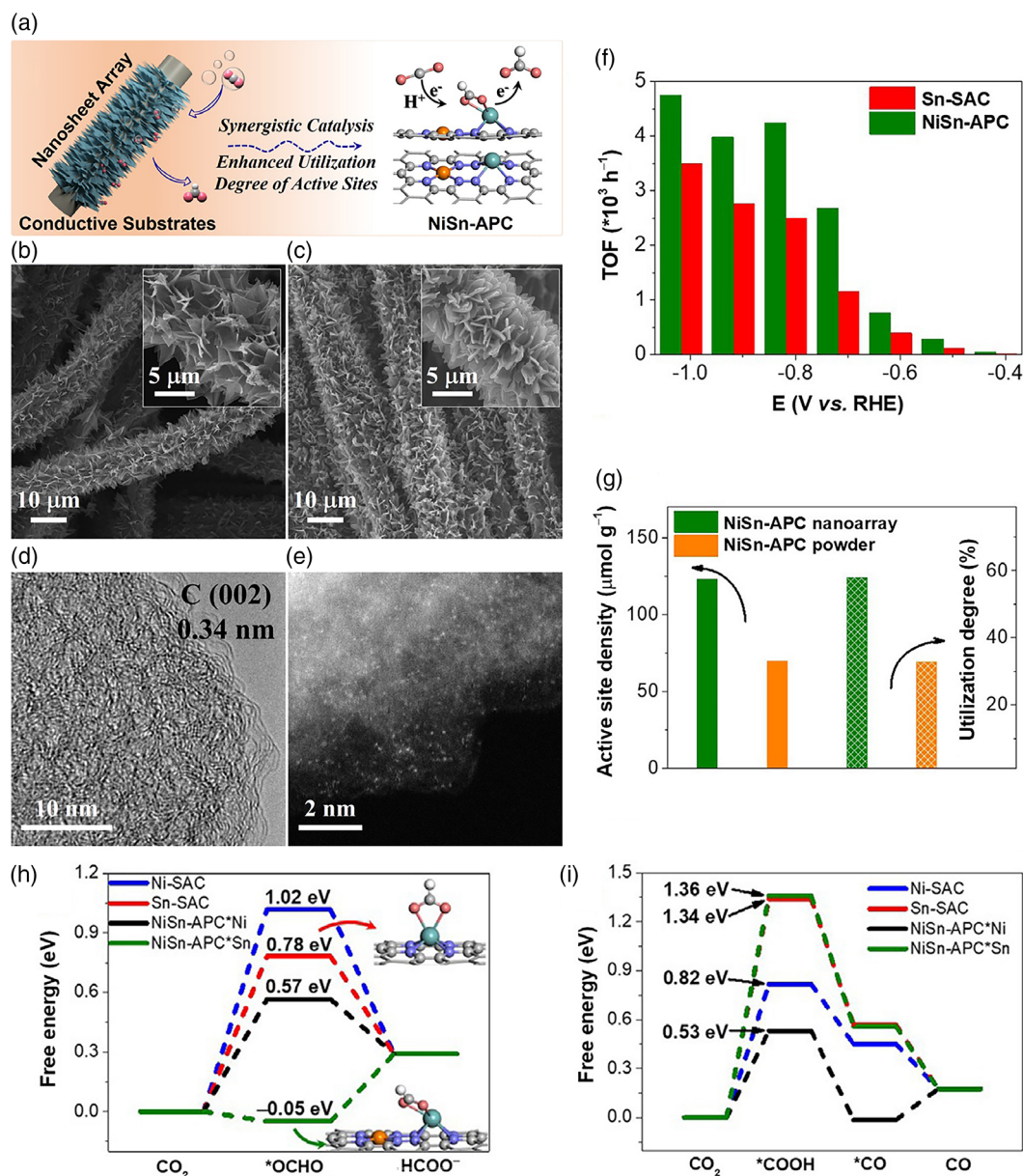


Figure 10. a) Scheme illustration for the integrated nanostructural NiSn atomic pair DAC (NiSn-APC) electrode and the CO_2 RR process on NiSn-APC. SEM images of b) N-doped carbon nanosheet and c) NiSn-APC nanoarray (insets are the corresponding magnified views). d) HRTEM and e) HAADF-STEM images of NiSn-APC. f) TOF values of Sn-SAC and NiSn-APC. g) Active site density and utilization degree of NiSn-APC, Ni-SAC nanoarray, and NiSn-APC powder. Free energy diagrams in CO_2 reduction reaction (CO_2 RR) for the production of h) formate and i) CO on Ni-SAC, Sn-SAC, NiSn-APC* Ni, and NiSn-APC* Sn. Scale bars are b) 10 μm , c) 10 μm , d) 10 nm, and e) 2 nm. Adapted with permission.^[78] Copyright 2020, Wiley-VCH.

capital-intensive because of the high bonding energy in N_2 ($\text{N}\equiv\text{N}$) molecules.^[14] Thus, rational design and engineering of high-performance NRR catalysts are of both fundamental and technological significance. DACs represent viable candidates. For instance, He et al.^[85] carried out DFT calculations and observed that the energy barriers of the first ($\Delta G_{\text{N}_2-\text{N}_2\text{H}}$) and second ($\Delta G_{\text{NH}_2-\text{NH}_3}$) proton-coupled electron-transfer steps could be reduced on the bimetal active sites; and in a series of metal combinations, Mo–Ru (0.17 eV), Mo–Co (0.27 eV), Mo–W (0.28 eV), Mo–Fe (0.36 eV), and Fe–Ru (0.39 eV) were found to

be the viable candidates for NRR electrocatalysis. Mechanistically, the strong polarization and weakening of the $\text{N}\equiv\text{N}$ bond were ascribed to the asymmetrical electron donation from the two different bimetallic active sites, as the binding strength of key reaction intermediates could be regulated by the synergistic interactions between the two metal centers, leading to an impressive NRR performance. Zheng et al.^[86] evaluated five DACs by DFT calculations, $\text{CrN}_4/\text{M}'\text{N}_4\text{-C}$ ($\text{M}' = \text{Cr, Mn, Fe, Cu, and Zn}$), where the CrN_4 moiety served as the main catalytic site, and the NRR catalytic activity was enhanced by the modulation

effect of the adjacent $M'N_4$ moiety, such that a remarkable NRR performance was achieved with the limiting potential ranging from -0.64 to -0.62 V. Wang et al.^[87] found that $FeMo/g-C_3N_4$ stood out as the optimal NRR catalyst with a particularly low limiting potential of -0.23 V based on the evaluations of 28 heteronuclear $M_1M_2/g-C_3N_4$ candidates. Nevertheless, thus far experimental progress of DACs for NRR electrocatalysis has remained slow and limited.

3.7. Other Reactions

DACs have also been found to exhibit a remarkable activity toward other reactions. For instance, Tian et al.^[23] prepared a $Fe_2/mpg-C_3N_4$ catalyst via a “precursor-preselected” wet-chemistry strategy. In this catalyst, highly dispersed Fe_2 clusters were supported on mesoporous carbon nitride ($mpg-C_3N_4$), which exhibited an excellent catalytic performance for the epoxidation of trans-stilbene to trans-stilbene oxide, with an outstanding selectivity of 93% at a high conversion efficacy of 91%. Li et al.^[88] synthesized a Fe_2N_6 catalyst by selecting uniform pyridinic N of graphitic carbon nitride ($g-C_3N_4$) as the anchoring sites. The peroxymonosulfate (PMS) activation performance was improved by 3.58 times and the selectivity of activating PMS via the radical pathway remained at a high level of 75%, due to the significantly improved PMS activation kinetics by the modified Fe_2CN catalyst. Because of the coupling of the Fe 3d orbitals, the contribution of the antibonding state in the Fe–O bond decreased by the new Fe–Fe coordination, which facilitated the O–O bond cleavage of the $Fe_2-HOO-SO_3$ complex with a thermodynamic energy barrier reduced to only -0.29 eV. This work confirms that the coordination configuration of the metal sites can significantly impact the intrinsic activity of DACs. In another study, Yang et al.^[89] synthesized a Ni–Ni DAC (Ni_1-N-C) for dehalogenation reactions via regulating the Ni content during sample synthesis. XAS, XPS, and HAADF-STEM measurements confirmed the diatomic structure of Ni_1-N-C . In the debromination reactions of tribromoacetic acid (TBAA), $Ni-N-C$ showed a higher intrinsic electrocatalytic activity than Ni, Ag, and Pd nanoparticles. Mechanistically, the unique adsorption configuration in $Ni-N-C$ led to a lower energy barrier than NiN_3 and NiN_4 SACs for the electrocatalytic debromination of TBAA.

4. Conclusion and Perspectives

Research of DACs has been increasingly intensified, where the more complicated materials structures offer a unique variable in the further manipulation of the electronic structure of the catalytic active sites, in comparison to SACs. The synergetic effect between the two metal atoms can be exploited for the control of the d-band centers and adsorption energetics of key reaction intermediates. This results in significant improvement of the electrocatalytic activities toward a variety of important reactions, such as HER, ORR, OER, CO_2RR , NRR, etc. In this review, we summarize the recent advances in the synthesis, characterization, and electrocatalytic performances and applications of a range of DACs. Yet, despite the progress, the research of DACs has remained in the rather early stage. Following are some of the challenges that need to be pursued in continuing research.

First, it has remained a great challenge to produce DACs with a uniform structure and atomic configuration. As mentioned earlier, in most syntheses, the products consist of a range of structures, including SAs, dual atoms, and even nanoclusters. Such a structural heterogeneity renders it challenging to unambiguously correlate the materials structure with the electrocatalytic activity, and to delineate their mechanistic contributions. Thus, development of effective protocols for high-yield, uniform production of DACs is urgently needed. Within this context, rational design of dinuclear organometallic complexes may be a viable strategy, along with controlled assembly onto a supporting substrate. This can be facilitated with the emerging ultrafast synthesis of electrocatalysts.^[90]

Second, the structural dynamics of the catalytic active sites have remained largely unexplored. One critical issue about DACs is if the dual-metal sites retain the dinuclear structure during electrochemical reactions, as structural instability can lead to diminishment of the electrocatalytic activity and compromise the long-term operation of the electrochemical devices. In fact, such issues of atomic restructuring have been observed with SACs.^[91–93] This calls for in situ, or better yet, operando, experimental tools to monitor the functional moieties.

Third, integration with state-of-the-art computational tools is of fundamental significance in catalyst design and structural engineering and critical to unravel the mechanistic insights. Specifically, a combinatorial approach may be adopted to identify viable pairing of the metal atoms as well as optimal atomic configurations within the dual-atom site.^[94] These insights can then serve as the guiding principle of the experimental design of DACs, where the two atomic sites may contribute additively or synergistically to the electrocatalytic activity.

Acknowledgements

This work was supported by the National Science Foundation (Grant nos. CHE-1900235 and CHE-2003685).

Conflict of Interest

The authors declare no conflict of interest.

Keywords

dual-atom catalysts, electrochemical energy conversion, electronic interaction, spin states, synergistic effects

Received: December 12, 2022

Revised: January 20, 2023

Published online:

- [1] M. T. M. Koper, Y. Iwasawa, *Phys. Chem. Chem. Phys.* **2014**, *16*, 13567.
- [2] Z. W. Chang, J. J. Xu, X. B. Zhang, *Adv. Energy Mater.* **2017**, *7*, 1700875.
- [3] L. G. Li, P. T. Wang, Q. Shao, X. Q. Huang, *Adv. Mater.* **2021**, *33*, 2004243.
- [4] Z. W. Chen, D. Higgins, A. P. Yu, L. Zhang, J. J. Zhang, *Energy Environ. Sci.* **2011**, *4*, 3167.

- [5] Y. J. Wang, B. Z. Fang, D. Zhang, A. J. Li, D. P. Wilkinson, A. Ignaszak, L. Zhang, J. J. Zhang, *Electrochem. Energy Rev.* **2018**, 1, 1.
- [6] B. Z. Lu, Q. M. Liu, S. W. Chen, *ACS Catal.* **2020**, 10, 7584.
- [7] Y. X. Wang, H. Y. Su, Y. H. He, L. G. Li, S. Q. Zhu, H. Shen, P. F. Xie, X. B. Fu, G. Y. Zhou, C. Feng, D. K. Zhao, F. Xiao, X. J. Zhu, Y. C. Zeng, M. H. Shao, S. W. Chen, G. Wu, J. Zeng, C. Wang, *Chem. Rev.* **2020**, 120, 12217.
- [8] X. B. Zheng, B. B. Li, Q. S. Wang, D. S. Wang, Y. D. Li, *Nano Res.* **2022**, 15, 7806.
- [9] Y. Peng, B. Z. Lu, S. W. Chen, *Adv. Mater.* **2018**, 30, 1801995.
- [10] B. T. Qiao, A. Q. Wang, X. F. Yang, L. F. Allard, Z. Jiang, Y. T. Cui, J. Y. Liu, J. Li, T. Zhang, *Nat. Chem.* **2011**, 3, 634.
- [11] Y. Chen, T. He, Q. Liu, Y. Hu, H. Gu, L. Deng, H. Liu, Y. Liu, Y.-N. Liu, Y. Zhang, S. Chen, X. Ouyang, *Appl. Catal., B* **2023**, 323, 122163.
- [12] N. C. Cheng, L. Zhang, K. Doyle-Davis, X. L. Sun, *Electrochem. Energy Rev.* **2019**, 2, 539.
- [13] E. Vorobyeva, E. Fako, Z. P. Chen, S. M. Collins, D. Johnstone, P. A. Midgley, R. Hauert, O. V. Safonova, G. Vile, N. Lopez, S. Mitchell, J. Perez-Ramirez, *Angew. Chem. Int. Ed.* **2019**, 58, 8724.
- [14] J. Zhang, Q. A. Huang, J. Wang, J. Wang, J. J. Zhang, Y. F. Zhao, *Chin. J. Catal.* **2020**, 41, 783.
- [15] H. M. Liu, H. P. Rong, J. T. Zhang, *Chemsuschem* **2022**, 15, 202200498.
- [16] Y. R. Ying, X. Luo, J. L. Qiao, H. T. Huang, *Adv. Funct. Mater.* **2021**, 31, 2007423.
- [17] R. Z. Li, D. S. Wang, *Adv. Energy Mater.* **2022**, 12, 2103564.
- [18] H. Yan, Y. Lin, H. Wu, W. H. Zhang, Z. H. Sun, H. Cheng, W. Liu, C. L. Wang, J. J. Li, X. H. Huang, T. Yao, J. L. Yang, S. Q. Wei, J. L. Lu, *Nat. Commun.* **2017**, 8, 1070.
- [19] S. E. Potts, H. B. Profijt, R. Roelofs, W. M. M. Kessels, *Chem. Vap. Deposition* **2013**, 19, 125.
- [20] E. Granneman, P. Fischer, D. Pierreux, H. Terhorst, P. Zagwijn, *Surf. Coat. Technol.* **2007**, 201, 8899.
- [21] L. Zhang, R. T. Si, H. S. Liu, N. Chen, Q. Wang, K. Adair, Z. Q. Wang, J. T. Chen, Z. X. Song, J. J. Li, M. N. Banis, R. Y. Li, T. K. Sham, M. Gu, L. M. Liu, G. A. Botton, X. L. Sun, *Nat. Commun.* **2019**, 10, 4936.
- [22] C. Xu, W. H. Yu, K. X. Zheng, C. Ling, S. T. Yu, L. Jiang, *J. Chem. Technol. Biotechnol.* **2020**, 95, 2187.
- [23] S. B. Tian, Q. Fu, W. X. Chen, Q. C. Feng, Z. Chen, J. Zhang, W. C. Cheong, R. Yu, L. Gu, J. C. Dong, J. Luo, C. Chen, Q. Peng, C. Draxl, D. S. Wang, Y. D. Li, *Nat. Commun.* **2018**, 9, 2353.
- [24] Y. T. He, X. X. Yang, Y. S. Li, L. T. Liu, S. W. Guo, C. Y. Shu, F. Liu, Y. N. Liu, Q. Tan, G. Wu, *ACS Catal.* **2022**, 12, 1216.
- [25] B. T. Hu, A. J. Huang, X. J. Zhang, Z. Chen, R. Y. Tu, W. Zhu, Z. B. Zhuang, C. Chen, Q. Peng, Y. D. Li, *Nano Res.* **2021**, 14, 3482.
- [26] C. C. Wu, X. M. Zhang, Z. X. Xia, M. Shu, H. Q. Li, X. L. Xu, R. Si, A. I. Rykov, J. H. Wang, S. S. Yu, S. L. Wang, G. Q. Sun, *J. Mater. Chem. A* **2019**, 7, 14001.
- [27] H. M. Yang, Y. Chen, Y. Qin, *Chin. J. Catal.* **2020**, 41, 227.
- [28] C. Z. Zhu, S. F. Fu, Q. R. Shi, D. Du, Y. H. Lin, *Angew. Chem. Int. Ed.* **2017**, 56, 13944.
- [29] F. Jaouen, E. Proietti, M. Lefevre, R. Chenitz, J. P. Dodelet, G. Wu, H. T. Chung, C. M. Johnston, P. Zelenay, *Energy Environ. Sci.* **2011**, 4, 114.
- [30] Y. Q. Wei, Y. Yang, M. Liu, Q. L. Li, Z. R. Huang, *J. Inorg. Mater.* **2020**, 35, 931.
- [31] Z. Y. Xiao, P. P. Sun, Z. L. Qiao, K. W. Qiao, H. X. Xu, S. T. Wang, D. P. Cao, *Chem. Eng. J.* **2022**, 446, 137112.
- [32] Y. Yang, Y. M. Qian, H. J. Li, Z. H. Zhang, Y. W. Mu, D. Do, B. Zhou, J. Dong, W. J. Yan, Y. Qin, L. Fang, R. F. Feng, J. G. Zhou, P. Zhang, J. C. Dong, G. H. Yu, Y. Y. Liu, X. M. Zhang, X. J. Fan, *Sci. Adv.* **2020**, 6, eaba6586.
- [33] S. Kandula, K. R. Shrestha, N. H. Kim, J. H. Lee, *Small* **2018**, 14, 1800291.
- [34] D. S. Yu, Y. C. Ma, F. Hu, C. C. Lin, L. L. Li, H. Y. Chen, X. P. Han, S. J. Peng, *Adv. Energy Mater.* **2021**, 11, 2101242.
- [35] Z. J. Liu, Q. Q. Jiang, R. L. Zhang, R. M. Gao, J. S. Zhao, *Electrochim. Acta* **2016**, 187, 81.
- [36] J. Wang, Z. Q. Huang, W. Liu, C. R. Chang, H. L. Tang, Z. J. Li, W. X. Chen, C. J. Jia, T. Yao, S. Q. Wei, Y. Wu, Y. D. Lie, *J. Am. Chem. Soc.* **2017**, 139, 17281.
- [37] C. Kubel, A. Voigt, R. Schoenmakers, M. Otten, D. Su, T. C. Lee, A. Carlsson, J. Bradley, *Microsc. Microanal.* **2005**, 11, 378.
- [38] K. Sohlberg, T. J. Pennycook, W. Zhou, S. J. Pennycook, *Phys. Chem. Chem. Phys.* **2015**, 17, 3982.
- [39] G. Z. Zhu, S. Prabhudev, J. Yang, C. M. Gabardo, G. A. Botton, L. Soleymani, *J. Phys. Chem. C* **2014**, 118, 22111.
- [40] C. Colliex, M. Tence, E. Lefevre, C. Mory, H. Gu, D. Bouchet, C. Jeanguillaume, *Mikrochim. Acta* **1994**, 114, 71.
- [41] M. L. Xiao, H. Zhang, Y. T. Chen, J. B. Zhu, L. Q. Gao, Z. Jin, J. J. Ge, Z. Jiang, S. L. Chen, C. P. Liu, W. Xing, *Nano Energy* **2018**, 46, 396.
- [42] Z. M. Xia, H. Zhang, K. C. Shen, Y. Q. Qu, Z. Jiang, *Physica B* **2018**, 542, 12.
- [43] T. He, Y. Chen, Q. M. Liu, B. Z. Lu, X. W. Song, H. T. Liu, M. Liu, Y. N. Liu, Y. Zhang, X. P. Ouyang, S. W. Chen, *Angew. Chem. Int. Ed.* **2022**, 61, e202201007.
- [44] K. I. Ozoemena, S. Chen, *Nanomaterials for Fuel Cell Catalysis*, 1st ed., Springer International Publishing: Imprint: Springer, Cham **2016**.
- [45] F. Ran, S. Chen, *Advanced Nanomaterials for Electrochemical Energy Conversion and Storage: Micro and Nano Technologies*, Elsevier, Amsterdam, Netherlands; Cambridge, MA **2020**.
- [46] N. N. Yuan, Q. Q. Jiang, Z. X. Wu, J. G. Tang, *J. Phys. Chem. C* **2020**, 124, 10804.
- [47] Q. Z. Xiong, Y. Wang, P. F. Liu, L. R. Zheng, G. Z. Wang, H. G. Yang, P. K. Wong, H. M. Zhang, H. J. Zhao, *Adv. Mater.* **2018**, 30, 1801450.
- [48] A. M. Harzandi, S. Shadman, M. Ha, C. W. Myung, D. Y. Kim, H. J. Park, S. Sultan, W. S. Noh, W. Lee, P. Thangavel, W. J. Byun, S. H. Lee, J. N. Tiwari, T. J. Shin, J. H. Park, Z. Lee, J. S. Lee, K. S. Kim, *Appl. Catal., B* **2020**, 270, 118896.
- [49] Z. X. Wu, Y. Zhao, W. P. Xiao, Y. L. Fu, B. H. Jia, T. Y. Ma, L. Wang, *ACS Nano* **2022**, 16, 18038.
- [50] W. L. Yu, Z. Chen, W. P. Xiao, Y. M. Chai, B. Dong, Z. X. Wu, L. Wang, *Inorg. Chem. Front.* **2022**, 9, 1847.
- [51] M. Kuang, Q. H. Wang, P. Han, G. F. Zheng, *Adv. Energy Mater.* **2017**, 7, 1700193.
- [52] Y. Zhou, E. H. Song, W. Chen, C. U. Segre, J. D. Zhou, Y. C. Lin, C. Zhu, R. G. Ma, P. Liu, S. F. Chu, T. Thomas, M. H. Yang, Q. Liu, K. Suenaga, Z. Liu, J. J. Liu, J. C. Wang, *Adv. Mater.* **2020**, 32, 2003484.
- [53] X. J. Zeng, J. L. Shui, X. F. Liu, Q. T. Liu, Y. C. Li, J. X. Shang, L. R. Zheng, R. H. Yu, *Adv. Energy Mater.* **2018**, 8, 1701345.
- [54] T. T. Cui, Y. P. Wang, T. Ye, J. Wu, Z. Q. Chen, J. Li, Y. P. Lei, D. S. Wang, Y. D. Li, *Angew. Chem. Int. Ed.* **2022**, 61, e202115219.
- [55] Y. O. Ma, H. Y. Fan, C. Wu, M. D. Zhang, J. H. Yu, L. Song, K. R. Li, J. P. He, *Carbon* **2021**, 185, 526.
- [56] L. C. Bai, C. S. Hsu, D. T. L. Alexander, H. M. Chen, X. L. Hu, *J. Am. Chem. Soc.* **2019**, 141, 14190.
- [57] S. Li, C. Cheng, X. J. Zhao, J. Schmidt, A. Thomas, *Angew. Chem. Int. Ed.* **2018**, 57, 1856.
- [58] M. K. Debe, *Nature* **2012**, 486, 43.
- [59] E. G. Luo, Y. Y. Chu, J. Liu, Z. P. Shi, S. Y. Zhu, L. Y. Gong, J. J. Ge, C. H. Choi, C. P. Liu, W. Xing, *Energy Environ. Sci.* **2021**, 14, 2158.
- [60] Y. Nie, L. Li, Z. D. Wei, *Chem. Soc. Rev.* **2015**, 44, 2168.
- [61] W. Xia, A. Mahmood, Z. B. Liang, R. Q. Zou, S. J. Guo, *Angew. Chem. Int. Ed.* **2016**, 55, 2650.
- [62] X. M. Ge, A. Sumboja, D. Wu, T. An, B. Li, F. W. T. Goh, T. S. A. Hor, Y. Zong, Z. L. Liu, *ACS Catal.* **2015**, 5, 4643.

- [63] L. Z. Zhang, J. M. T. A. Fischer, Y. Jia, X. C. Yan, W. Xu, X. Y. Wang, J. Chen, D. J. Yang, H. W. Liu, L. Z. Zhuang, M. Hanke, D. J. Searles, K. K. Huang, S. H. Feng, C. L. Brown, X. D. Yao, *J. Am. Chem. Soc.* **2018**, *140*, 10757.
- [64] S. Samireddi, V. Aishwarya, I. Shown, S. Muthusamy, S. M. Unni, K. T. Wong, K. H. Chen, L. C. Chen, *Small* **2021**, *17*, 2103823.
- [65] Z. Y. Chen, X. Z. Su, J. Ding, N. Yang, W. B. Zuo, Q. Y. He, Z. M. Wei, Q. Zhang, J. Huang, Y. M. Zhai, *Appl. Catal., B* **2022**, *308*, 121206.
- [66] R. Mercado, C. Wahl, J. E. Lu, T. J. Zhang, B. Z. Lu, P. Zhang, J. N. Q. Lu, A. Allen, J. Z. Zhang, S. W. Chen, *Chemcatchem* **2020**, *12*, 3230.
- [67] Y. G. Li, H. J. Dai, *Chem. Soc. Rev.* **2014**, *43*, 5257.
- [68] N. N. Xu, J. L. Qiao, *J. Electrochem.* **2020**, *26*, 531.
- [69] Y. X. Gao, D. B. Zheng, Q. C. Li, W. P. Xiao, T. Y. Ma, Y. L. Fu, Z. X. Wu, L. Wang, *Adv. Funct. Mater.* **2022**, *32*, 2203206.
- [70] Z. X. Wu, H. B. Wu, T. F. Niu, S. Wang, G. T. Fu, W. Jin, T. Y. Ma, *ACS Sustainable Chem. Eng.* **2020**, *8*, 9226.
- [71] Y. Y. Wu, C. C. Ye, L. Yu, Y. F. Liu, J. F. Huang, J. B. Bi, L. Xue, J. W. Sun, J. Yang, W. Q. Zhang, X. Wang, P. Xiong, J. W. Zhu, *Energy Storage Mater.* **2022**, *45*, 805.
- [72] M. H. Li, H. F. Wang, W. Luo, P. C. Sherrell, J. Chen, J. P. Yang, *Adv. Mater.* **2020**, *32*, 2001848.
- [73] D. Siltamaki, S. Chen, F. Rahmati, J. Lipkowski, A. C. Chen, *J. Electrochem.* **2021**, *27*, 278.
- [74] Y. F. Li, C. Chen, R. Cao, Z. W. Pan, H. He, K. B. Zhou, *Appl. Catal., B* **2020**, *268*, 118747.
- [75] N. Q. Zhang, X. X. Zhang, Y. K. Kang, C. L. Ye, R. Jin, H. Yan, R. Lin, J. R. Yang, Q. Xu, Y. Wang, Q. H. Zhang, L. Gu, L. C. Liu, W. Y. Song, J. Liu, D. S. Wang, Y. D. Li, *Angew. Chem. Int. Ed.* **2021**, *60*, 13388.
- [76] Y. Wang, B. J. Park, V. K. Paidi, R. Huang, Y. C. Lee, K. J. Noh, K. S. Lee, J. W. Han, *ACS Energy Lett.* **2022**, *7*, 640.
- [77] X. Y. Cao, L. L. Zhao, B. R. Wulan, D. X. Tan, Q. W. Chen, J. Z. Ma, J. T. Zhang, *Angew. Chem. Int. Ed.* **2022**, *61*, e202113918.
- [78] W. F. Xie, H. Li, G. Q. Cui, J. B. Li, Y. K. Song, S. J. Li, X. Zhang, J. Y. Lee, M. F. Shao, M. Wei, *Angew. Chem. Int. Ed.* **2021**, *60*, 7382.
- [79] W. H. Ren, X. Tan, W. F. Yang, C. Jia, S. M. Xu, K. X. Wang, S. C. Smith, C. Zhao, *Angew. Chem. Int. Ed.* **2019**, *58*, 6972.
- [80] L. Z. Meng, E. H. Zhang, H. Y. Peng, Y. Wang, D. S. Wang, H. P. Rong, J. T. Zhang, *ChemCatChem* **2022**, *14*, e202101801.
- [81] H. Y. Cheng, X. M. Wu, M. M. Feng, X. C. Li, G. P. Lei, Z. H. Fan, D. W. Pan, F. J. Cui, G. H. He, *ACS Catal.* **2021**, *11*, 12673.
- [82] C. G. Morales-Guio, E. R. Cave, S. A. Nitopi, J. T. Feaster, L. Wang, K. P. Kuhl, A. Jackson, N. C. Johnson, D. N. Abram, T. Hatsukade, C. Hahn, T. F. Jaramillo, *Nat. Catal.* **2018**, *1*, 764.
- [83] B. W. Zhou, P. F. Ou, N. Pant, S. B. Cheng, S. Vanka, S. Chu, R. T. Rashid, G. Botton, J. Song, Z. T. Mi, *Proc. Natl. Acad. Sci. USA* **2020**, *117*, 1330.
- [84] L. M. Azofra, *Curr. Opin. Electrochem.* **2022**, *35*, 101073.
- [85] T. W. He, A. R. P. Santiago, A. J. Du, *J. Catal.* **2020**, *388*, 77.
- [86] X. N. Zheng, Y. Liu, Y. Yan, X. X. Li, Y. Yao, *Chin. Chem. Lett.* **2022**, *33*, 1455.
- [87] S. Y. Wang, L. Shi, X. W. Bai, Q. Li, C. Y. Ling, J. L. Wang, *ACS Cent. Sci.* **2020**, *6*, 1762.
- [88] J. Li, Y. X. Zou, Z. F. Li, S. H. Fu, Y. Lu, S. Y. Li, X. B. Zhu, T. T. Zhang, *ACS Appl. Mater. Interfaces* **2022**, *14*, 37865.
- [89] B. Yang, H. B. Li, Z. R. Zhang, K. Xiao, M. T. Yang, F. Z. Zhang, M. M. Wang, X. Guo, Q. X. Li, W. Fu, R. Si, L. Z. Wang, H. H. Chen, *Chem. Eng. J.* **2022**, *427*, 131719.
- [90] S. B. Zhang, Y. F. Wu, Y. X. Zhang, Z. Q. Niu, *Sci. China Chem.* **2021**, *64*, 1908.
- [91] J. Yang, H. F. Qi, A. Q. Li, X. Y. Liu, X. F. Yang, S. X. Zhang, Q. Zhao, Q. K. Jiang, Y. Su, L. L. Zhang, J. F. Li, Z. Q. Tian, W. Liu, A. Q. Wang, T. Zhang, *J. Am. Chem. Soc.* **2022**, *144*, 12062.
- [92] D. Karapinar, N. T. Huan, N. R. Sahraie, J. K. Li, D. Wakerley, N. Touati, S. Zanna, D. Taverna, L. H. G. Tizei, A. Zitolo, F. Jaouen, V. Mougel, M. Fontecave, *Angew. Chem. Int. Ed.* **2019**, *58*, 15098.
- [93] H. Xu, D. Rebollar, H. He, L. Chong, Y. Liu, C. Liu, C.-J. Sun, T. Li, J. V. Muntean, R. E. Winans, D.-J. Liu, T. Xu, *Nat. Energy* **2020**, *5*, 623.
- [94] Y. A. Zhou, L. L. Chen, L. Sheng, Q. Q. Luo, W. H. Zhang, J. L. Yang, *Nano Res.* **2022**, *15*, 7994.



Tianchen Cui received his B.S. degree in applied chemistry in 2022 from Dalian University of Technology, Liaoning, China. He then went on to the University of California at Santa Cruz (UCSC) to pursue a Ph.D. degree in chemistry under the supervision of Professor Shaowei Chen. His dissertation research focuses on dual-atom catalysts toward electrochemical energy conversion, ligand functionalization of nanoparticles, and ultrafast synthesis of electrocatalysts.



Qiming Liu received his B.E. degree in materials chemistry in 2018 from Central South University, Hunan, China. He then joined Professor Shaowei Chen's group at UCSC to pursue a Ph.D. degree in chemistry. His research interests concentrate on the design and engineering of nanocomposite catalysts for electrochemical energy conversion, development of ultrafast synthesis, and ligand functionalization of nanoparticles.



Shaowei Chen finished his undergraduate study in 1991 with a B.S. degree in chemistry from the University of Science and Technology of China (USTC), and then went to Cornell University receiving his M.S. and Ph.D. degrees in 1993 and 1996, respectively. Following a postdoctoral appointment in the University of North Carolina at Chapel Hill, he started his independent career in Southern Illinois University in 1998. In summer 2004, he moved to UCSC, and is currently a professor of chemistry and the faculty director of the UCSC COSMOS program.